Neuron

Article

Functional coupling of TRPM2 and extrasynaptic NMDARs exacerbates excitotoxicity in ischemic brain injury

Graphical abstract

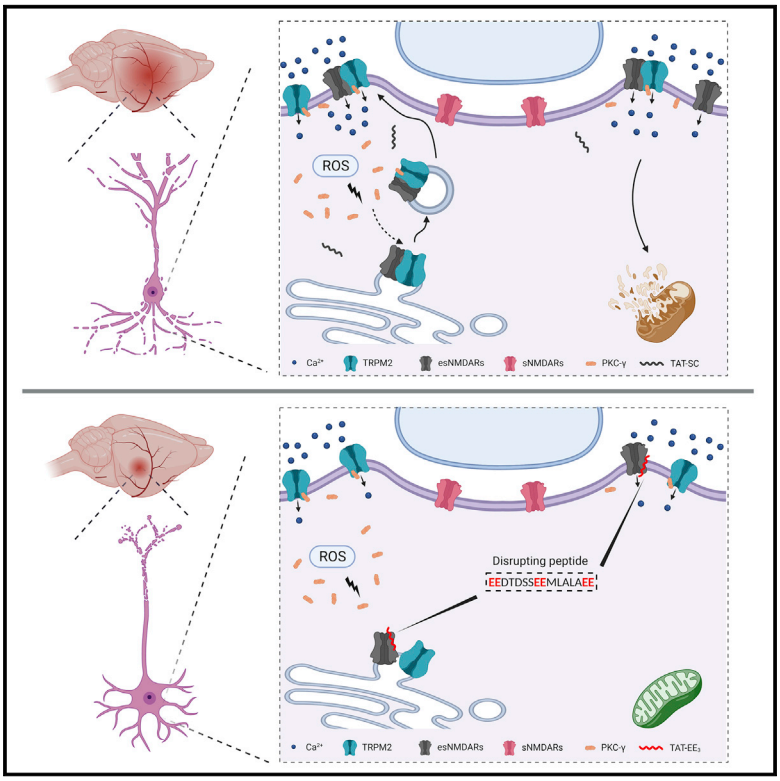

Highlights

- TRPM2 physically and functionally interacts with extrasynaptic NMDAR
- TRPM2-NMDAR interaction exacerbates excitotoxicity during ischemic stroke
- TRPM2 recruits PKCγ, thereby increasing NMDAR's surface expression
- Uncoupling TRPM2-NMDAR interaction attenuates ischemic brain injury

Authors

Pengyu Zong, Jianlin Feng, Zhichao Yue, ..., Yasuo Mori, Bing Hao, Lixia Yue

Correspondence

lyue@uchc.edu

In brief

Zong et al. discover an unexpected association between the oxidative stress-sensitive ion channel TRPM2 and the extrasynaptic NMDA receptor (NMDAR) in the neurons, which enhances excitotoxicity during ischemic brain injury. Neuron-specific knockout of TRPM2 or uncoupling of the TRPM2-NMDAR association using an interfering peptide protects mice against ischemic stroke.

Zong et al., 2022, Neuron *110*, 1944–1958
June 15, 2022
https://doi.org/10.1016/j.neuron.2022.03.021

CellPress

CellPress

Neuron

Article

Functional coupling of TRPM2 and extrasynaptic NMDARs exacerbates excitotoxicity in ischemic brain injury

Pengyu Zong,[1] Jianlin Feng,[1] Zhichao Yue,[1] Yunfeng Li,[2] Gongxiong Wu,[3] Baonan Sun,[1] Yanlin He,[1] Barbara Miller,[4] Albert S. Yu,[1] Zhongping Su,[1] Jia Xie,[1] Yasuo Mori,[5,6] Bing Hao,[2] and Lixia Yue[1,7,*]

[1]Department of Cell Biology, Calhoun Cardiology Center, University of Connecticut School of Medicine (UConn Health), Farmington, CT 06030, USA

[2]Department of Molecular Biology and Biophysics, University of Connecticut School of Medicine (UConn Health), Farmington, CT 06030, USA

[3]Department of Medicine, Brigham and Women's Hospital, Laboratory for Translational Research, Harvard Medical School, Cambridge, MA 02139, USA

[4]Departments of Pediatrics and Biochemistry and Molecular Biology, The Pennsylvania State University College of Medicine, P.O. Box 850, Hershey, PA 17033, USA

[5]Laboratory of Molecular Biology, Department of Synthetic Chemistry and Biological Chemistry, Graduate School of Engineering, Kyoto University, Kyoto 615-8510, Japan

[6]The World Premier International Research Initiative, Institute for Integrated Cell-Material Sciences, Kyoto University, Kyoto 615-8510, Japan

[7]Lead contact

*Correspondence: lyue@uchc.edu

https://doi.org/10.1016/j.neuron.2022.03.021

SUMMARY

Excitotoxicity induced by NMDA receptor (NMDAR) activation is a major cause of neuronal death in ischemic stroke. However, past efforts of directly targeting NMDARs have unfortunately failed in clinical trials. Here, we reveal an unexpected mechanism underlying NMDAR-mediated neurotoxicity, which leads to the identification of a novel target and development of an effective therapeutic peptide for ischemic stroke. We show that NMDAR-induced excitotoxicity is enhanced by physical and functional coupling of NMDAR to an ion channel TRPM2 upon ischemic insults. TRPM2-NMDAR association promotes the surface expression of extrasynaptic NMDARs, leading to enhanced NMDAR activity and increased neuronal death. We identified a specific NMDAR-interacting motif on TRPM2 and designed a membrane-permeable peptide to uncouple the TRPM2-NMDAR interaction. This disrupting peptide protects neurons against ischemic injury *in vitro* and protects mice against ischemic stroke *in vivo*. These findings provide an unconventional strategy to mitigate excitotoxic neuronal death without directly targeting NMDARs.

INTRODUCTION

Ischemic stroke is a leading cause of disability and mortality worldwide (Virani et al., 2020). Numerous factors are involved in neuronal damage during ischemic stroke, among which Ca^{2+} overload plays a key role (Granzotto et al., 2020). Ca^{2+} overload caused by excitotoxic mechanisms through NMDA receptor (NMDAR) activation and subsequent activation of nonglutamatergic Ca^{2+}-permeable channels (Tymianski, 2011) triggers a series of downstream cytotoxic events, including reactive oxygen species (ROS) generation, mitochondrial dysfunction, and necrosis/apoptosis cascade activation, which ultimately leads to neuronal death (Choi, 2020). NMDAR-mediated excitotoxicity has been extensively studied since its first discovery 50 years ago (Olney, 1969). However, NMDAR antagonists all failed to attenuate ischemic stroke in human patients (Sena et al., 2007).

Failure of NMDAR antagonists shifted focus of neuroprotection research in ischemic stroke toward identifying the downstream intracellular signaling pathways triggered by NMDARs (Wu and Tymianski, 2018), and the investigation of subtype-dependent (Ge et al., 2020), as well as localization-dependent, excitotoxic effects of NMDARs (Hardingham and Bading, 2010). Over a third of surface NMDARs are located extrasynaptically (Petit-Pedrol and Groc, 2021) and closely related to neurotoxicity. In contrast, activation of synaptic NMDARs promotes neuron survival through activation of the extracellular signal-regulated kinase (ERK) and cAMP response element-binding protein (CREB) signaling pathways (Bading, 2013; Hardingham, 2019). Moreover, several nonglutamatergic Ca^{2+}-permeable channels in neurons have recently been suggested as potential therapeutic targets (Tymianski, 2011), including TRPM2 (Belrose and Jackson, 2018).

TRPM2 was discovered as an oxidative stress sensitive Ca^{2+}-permeable channel (Hara et al., 2002; Perraud et al., 2001; Sano

et al., 2001) that is gated by elevated intracellular Ca^{2+} and ADP ribose (ADPR) (Huang et al., 2019; Wang et al., 2018; Zhang et al., 2018) and can also be regulated by different stress factors such as acidic pH (Du et al., 2009b; Starkus et al., 2010; Yang et al., 2010), glutathione (Belrose et al., 2012), Zn^{2+} (Mortadza et al., 2017), and heat (Kashio et al., 2012). TRPM2 is abundantly expressed in the brain (Fonfria et al., 2006) and is involved in neuronal death caused by oxidative stress (Belrose and Jackson, 2018; Mai et al., 2020). Contribution of TRPM2 to ischemic brain injury was initially indicated by TRPM2 knockdown (Jia et al., 2011) and was later demonstrated in TRPM2 global knockout mice (Alim et al., 2013; Gelderblom et al., 2014; Shimizu et al., 2013). It was also reported that TRPM2 in immunocompetent cells plays a critical role in ischemic stroke (Gelderblom et al., 2014). Thus, the mechanisms by which TRPM2 results in deleterious effects in ischemic stroke remain elusive (Belrose and Jackson, 2018; Mai et al., 2020). More importantly, it was unknown whether TRPM2 is involved in excitotoxicity in ischemic stroke. Given the complexity of excitotoxicity, which includes overactivation of glutamatergic NMDARs and subsequent activation of nonglutamatergic Ca^{2+}-permeable channels, a mechanism that can influence NMDARs' excitotoxicity and its downstream pathways may be an ideal candidate target for ischemic stroke to produce better therapeutic outcomes. As TRPM2 activation requires elevated intracellular Ca^{2+}/ADPR, which can be produced subsequent to NMDARs' activation during ischemic stroke, we reasoned that TRPM2 may influence NMDARs' excitotoxicity.

Here, we unveil a previously unknown mechanism by which TRPM2 mediates neuronal death during ischemic stroke. We found that TRPM2 exacerbates NMDARs' excitotoxicity by physically and functionally interacting with NMDARs. We identified the interacting motifs and designed a disruptive peptide TAT-EE_3, which can uncouple TRPM2-NMDARs interaction, thereby protecting neurons against ischemic injury *in vitro* and *in vivo*. Our findings establish that TRPM2 exacerbates extrasynaptic NMDARs' excitotoxicity; therefore, intervention of TRPM2-NMDAR coupling may represent a promising therapeutic strategy for ischemic stroke.

RESULTS

TRPM2 deletion in neurons protects mice against ischemic stroke

Neuron-specific *Trpm2* deletion was achieved by crossing nestin-cre mice with $Trpm2^{fl/fl}$ mice, which was confirmed by PCR, western blot (WB), and current recording (Figures S1A–S1K). Successful middle cerebral artery occlusion (MCAO) was confirmed by monitoring blood flow reduction by 85% (Figures S1L–S1M). Similar to global *Trpm2* knockout (gM2KO), neuron-specific *Trpm2* deletion (Cre^+, $Trpm^{fl/fl}$; nM2KO) exhibited reduced infarct volume and improved neurological performance compared with control (Cre^-, $Trpm2^{fl/fl}$; wild-type [WT]) littermates (Figures 1A–1D). Apoptosis is an important cause of neuronal death. In the penumbra after MCAO (Figure S1N), the number of TUNEL-positive neurons was markedly smaller in brain slices from gM2KO and nM2KO than those of control littermates (Figures 1E–1H, S1O, and S1P). These results suggest that neuronal TRPM2 plays a key role in causing ischemic brain damage.

Besides apoptosis, Ca^{2+} overload also causes necrosis in neurons (Choi, 1995). Using isolated cortical neurons, we performed oxygen-glucose deprivation (OGD) to mimic *in vivo* ischemic injury. OGD induced a persistent increase of $[Ca^{2+}]_i$ (Figures 1I and 1J), until the lysis of neurons, as reflected by a complete loss of Fura-2 fluorescence (Figure 1I; see the arrow-pointed cells). The lysed neurons were counted as dead neurons. Throughout the 90 min of OGD exposure, a notable number of neurons (6.8%) in the WT group died after 30 min of OGD, which was increased to 35.2% and 58.5% at 60 and 90 min (Figures 1I–1L). In contrast, only 1.9%, 8.7%, and 16.3% of neurons died at 30, 60, and 90 min in the gM2KO group, respectively (Figure 1L). Also, the increase of $[Ca^{2+}]_i$ was remarkably higher in WT than in gM2KO neurons (Figures 1I–1L). Similar results were also observed in neurons isolated from nM2KO mice (Figures S2A–S2D). During OGD, 80% of the Ca^{2+} entry in neurons is mediated by NMDARs (Goldberg and Choi, 1993; Lipton, 1999). Indeed, NMDAR blockers, AP5 and MK801, inhibited the increase of $[Ca^{2+}]_i$ and neuronal death induced by OGD in WT neurons, but there was no further reduction in gM2KO neurons (Figures S2E–S2H). Mitochondrial dysfunction is an early event promoting neuronal death (Lemasters et al., 2009). We found that OGD induced mitochondrial depolarization in WT neurons as indicated by increased Rh123 fluorescence, but this increase was largely prevented by *Trpm2* deletion (Figures 1M and 1N), NMDAR blockers AP5 or MK-801, removing extracellular Ca^{2+}, or chelating intracellular Ca^{2+} using BAPTA-AM (Figures S2I–S2L). These results suggest a critical role of TRPM2 in aggregating NMDAR-mediated Ca^{2+} overload, mitochondrial dysfunction, and neuronal death during OGD.

We next examined whether TRPM2 in neurons can be activated by OGD. Suboptimal Ca^{2+} and ADPR concentrations (Du et al., 2009a) in the pipette solution were used for TRPM2 recording (Figure S1Q). During OGD, TRPM2 current was elicited in neurons from WT mice (Figures 1O–1Q), but not in the neurons from *Trpm2* deletion mice (Figures 1O, bottom, and 1Q). We also found that TRPM2 expression in the brain was markedly upregulated by MCAO (Figures S1R–S1S). Moreover, MCAO-induced increase of NMDARs' surface expression was inhibited by *Trpm2* deletion (Figures 1R and 1S). Importantly, the effects of TRPM2 on NMDAR's surface expression were specific, as the surface expressions of other membrane proteins such as TRPM4 and pannexin-1 were not influenced by *Trpm2* deletion (Figures S2M and S2N). The above data suggest that the upregulation of TRPM2 expression is important for the increase of NDMARs' surface expression after ischemic stroke.

TRPM2 interacts with NMDARs

To understand how TRPM2 influences NMDARs' surface expression, we examined whether TRPM2 interacts with NMDARs and found that TRPM2 can be coimmunoprecipitated by GluN1a, GluN2a, and GluN2b in the HEK293T overexpression system (Luo et al., 2002; Schmitz et al., 2003) (Figure 2A). Reciprocally, GluN1a, GluN2a, and GluN2b can also be coimmunoprecipitated by TRPM2 (Figure 2B). Interestingly, when transfected with GluN1a, GluN2a, or GluN2b separately, TRPM2 can be only coimmunoprecipitated with GluN2a and GluN2b, but not GluN1a

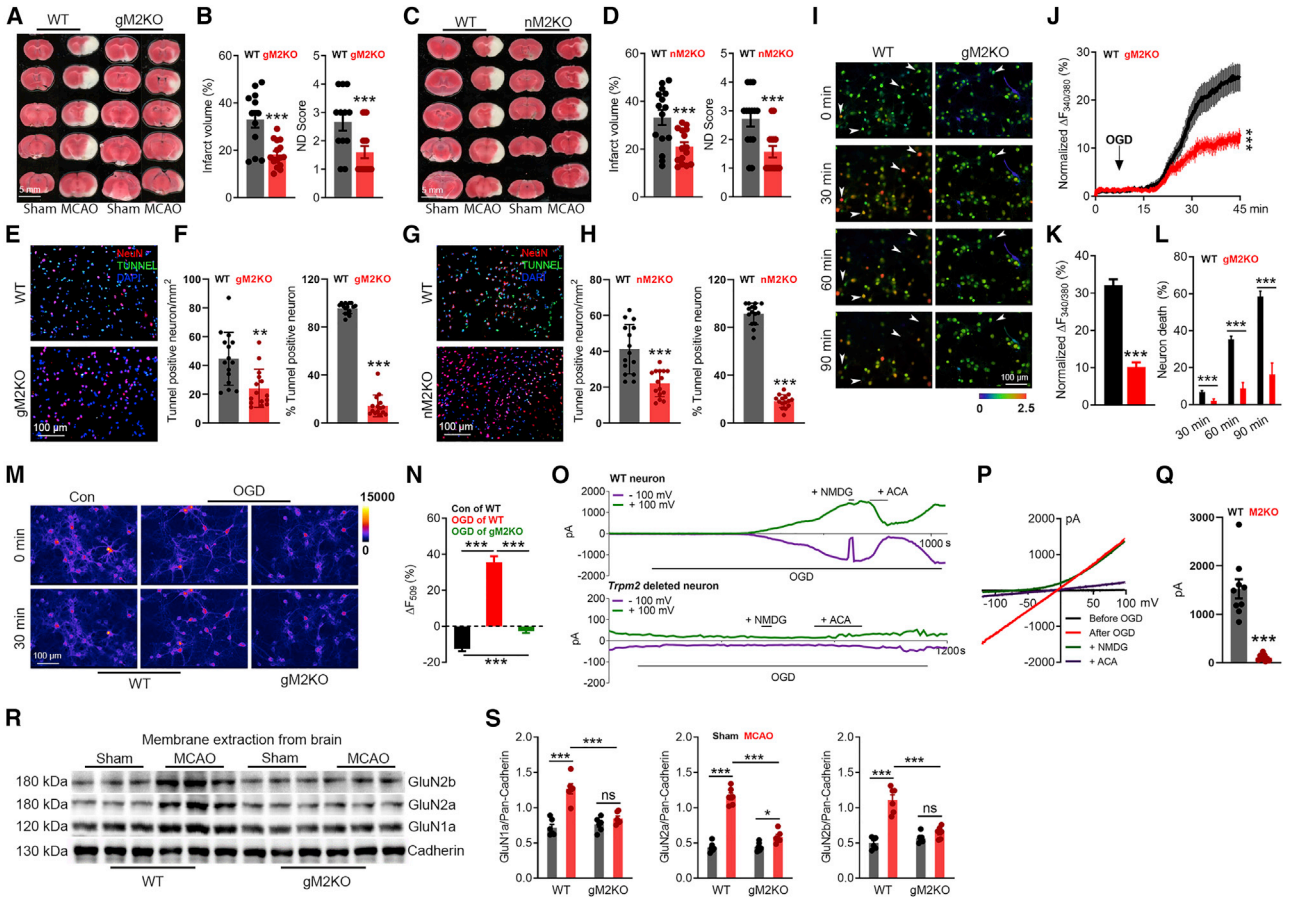

Figure 1. Neuron-specific *Trpm2* deletion protects the brain against ischemic damage

(A and B) Global *Trpm2* deletion (gM2KO) attenuates ischemic stroke. (A) TTC staining of brain slices of wild-type (WT) and gM2KO mice 24 h after MCAO. Average infarct volume (B, left) and ND score (B, right) (n = 12 for WT and 15 for gM2KO).

(C and D) Neuron-specific *Trpm2* deletion (nM2KO) produces similar protective effects as that of gM2KO. (C) TTC staining of nM2KO and Cre^{-} control littermates (WT) 24 h after surgery. Average infarct volume (D, left) and ND score (D, right) (n = 15 for WT and 15 for nM2KO).

(E–H) TUNEL staining of the penumbra (Figure S1N) in brain sections from gM2KO (E and F) and nM2KO (G and H) mice. (E and G) Merged images (red, NeuN; blue, DAPI; and green, TUNEL). (F and H) Quantification of TUNEL-positive neurons and mean percentage of TUNNEL positive neurons in all NeuN-positive cells (n = 5/group).

(I–L) Ratio Ca^{2+} imaging. (I) Arrows indicate representative lysed neurons with increasing intracellular Ca^{2+}. (J) Averaged Ca^{2+} imaging traces (n = 20/group). (K) Quantification of OGD-induced Fura-2 fluorescence changes (n = 238/6 dishes for WT and 233/6 dishes for gM2KO). (L) OGD-induced neuronal death (n = 6/group).

(M and N) R123 imaging. (M) R123-labeled mitochondria before and 30 min after OGD. Control group (no OGD treatment) was used to show the rapid photobleaching of R123. (N) Quantification of R123 fluorescence change (n = 39, 74, 123, respectively).

(O–Q) OGD-induced TRPM2 activation in WT neurons. (O) Time-dependent current activation and blockade by ACA. NMDG was used to ensure the tight seal. (P) I-V relationship. (Q) Average of current amplitudes.

(R and S) WB for surface expression of NMDARs in the brain (n = 12/group).

ns, no statistical significance, *p < 0.05, **p < 0.01, ***p < 0.001; ANOVA, Bonferroni's test; mean ± SEM.

(Figure 2C), indicating that in NMDARs, GluN2a and GluN2b interact with TRPM2. We further confirmed the presence of TRPM2-NMDAR association in the brain lysates (Figures 2D and 2E). To determine the consequences of TRPM2-NMDAR association, we found that NMDAR currents were much bigger in WT neurons (Figures 2F and 2G) and in NMDARs/TRPM2 coexpressing HEK293 cells (Figures 2J and 2K) than that in the TRPM2-KO neurons and NMDARs/EGFP coexpressing cells, respectively. Similarly, surface expression of NMDAR was higher in NMDARs/TRPM2 than that in NMDARs/EGFP-expressing cells (Figures 2H and 2I). The increased surface expression and enhanced NMDAR currents were also observed when GluN1a/GluN2a or GluN1a/GluN2b was separately transfected with TRPM2 (Figures S3A–S3H). Moreover, both the current amplitude and surface expression of TRPM2 were also increased when TRPM2 was coexpressed with NMDARs (Figures S3I–S3L). These results suggest that the physical interaction between TRPM2 and NMDARs produces functional consequences.

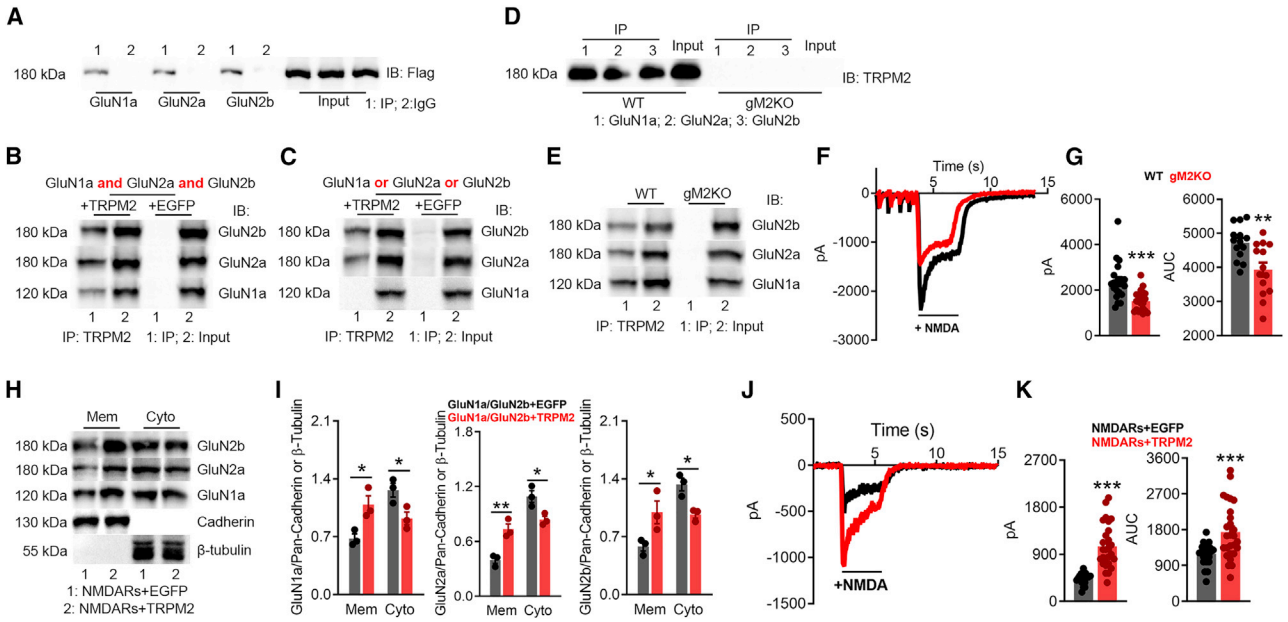

Figure 2. TRPM2 physically and functionally interacts with NMDARs

(A and B) CoIP of NMDARs and TRPM2 expressed in HEK-293T cells. (A) IP using anti-NMDARs and immunoblotting (IB) with anti-Flag. (B) IP using anti-Flag and IB with anti-NMDARs.

(C) CoIP of TRPM2 coexpressed with GluN1a, GluN2a, or GluN2b in HEK-293T cells. IP using anti-Flag and IB with anti-NMDARs.

(D and E) CoIP of NMDARs and TRPM2 in the brain lysates. (D) IP using anti-NMDARs and IB with anti-TRPM2. (E) IP using anti-TRPM2 and IB with anti-NMDARs.

(F and G) NMDAR current recording from isolated WT and gM2KO neurons. (G) Average peak current amplitude and area under curve (AUC) (n = 20/group).

(H and I) Surface expression of NMDARs in HEK-293T cells cotransfected with NMDARs/TRPM2 or NMDARs/EGFP plasmids. Membrane (Mem) and cytosol (Cyto) protein levels assessed with WB.

(J and K) NMDAR current recording from HEK293T cells transfected with NMDARs/TRPM2 or NMDARs/EGFP. (K) Average peak current amplitude and AUC from NMDARs/EGFP group (n = 23) and NMDARs/TRPM2 group (n = 27).

*p < 0.05, **p < 0.01, ***p < 0.001; ANOVA, Bonferroni's test; mean ± SEM.

Identification of the interaction motifs in NMDARs and TRPM2

N- and C-tail fragments of TRPM2 were subcloned and tagged with FLAG and GFP, respectively. When coexpressed with NMDARs, the TRPM2-NT, but not the TRPM2-CT, was detected in the immunoprecipitates of anti-NMDAR (Figures 3A and 3B). For NMDARs, the C-tails of GluN2a and GluN2b were generated and tagged with GFP and showed interaction with TRPM2, whereas the GFP-tagged C-tail deleted GluN2a (GluN2a−ΔCT) and GluN2b (GluN2b−ΔCT) were absent in the immunoprecipitates of anti-TRPM2 (Figure 3C). Moreover, TRPM2-NT produced a similar potentiation on NMDAR current and NMDA-induced Ca^{2+} entry as the full-length TRPM2 (TRPM2-FL) (Figures 3D and 3E). These findings suggest that the C termini of GluN2a and GluN2b interact with TRPM2's N-terminal domain. To narrow down the NMDAR-interacting domain in TRPM2-NT (Figure 3F), we generated a series of truncation constructs by incrementally deleting about 50 residues. We found that the N-terminal amino acid residues from 631 to 679 are critical for the TRPM2-NMDAR interaction (Figures 3G–3I), as both forward and reverse coimmunoprecipitation (coIP) experiments confirmed the interaction of NMDARs with the fragments of 1–727 and 1–679, whereas the fragments shorter than 631 residues failed to interact with NMDARs. We further shortened the 1–679 fragment and found that the region between residues 665 and 679 is the minimal sequence required for the TRPM2-NMDAR interaction (Figures 3J–3L).

Interestingly, the 15 residues between 665 and 679 contain two "glutamate-glutamate" (EE) repeats separated by five residues and followed by another EE repeat (Figure 3F); hence, we denoted the sequence between 665 to 681 the "EE_3" motif for simplicity. This EE_3 motif is conserved in TRPM2 from different species but was absent in all other TRPM channels (Figures S4A–S4B). When the EE_3 motif was deleted from the full-length TRPM2 (TRPM2-ΔEE3), interaction between TRPM2 and NMDARs disappeared (Figure 3M). Intriguingly, when the middle "EE" of the EE_3 motif was replaced by two glutamine residues ("QQ"), the resulting TRPM2-EQE mutant failed to interact with NMDARs, whereas the replacements of the first and third EE repeats (TRPM2-QEE and TRPM2-EEQ) did not influence the TRPM2-NMDAR interaction (Figure 3O). Consistent with the disrupted interaction, TRPM2-ΔEE3 and TRPM2-EQE mutants failed to enhance NMDAR currents, whereas TRPM2-QEE and TRPM2-EEQ mutants produced an effect similar to TRPM2-WT (Figures 3N and 3P). Importantly, these mutants exhibited similar electrophysiological properties as TRPM2-WT (Figures S4C–S4H). These results indicate that the EE_3 motif is essential for both the physical and functional coupling between TRPM2 and NMDARs.

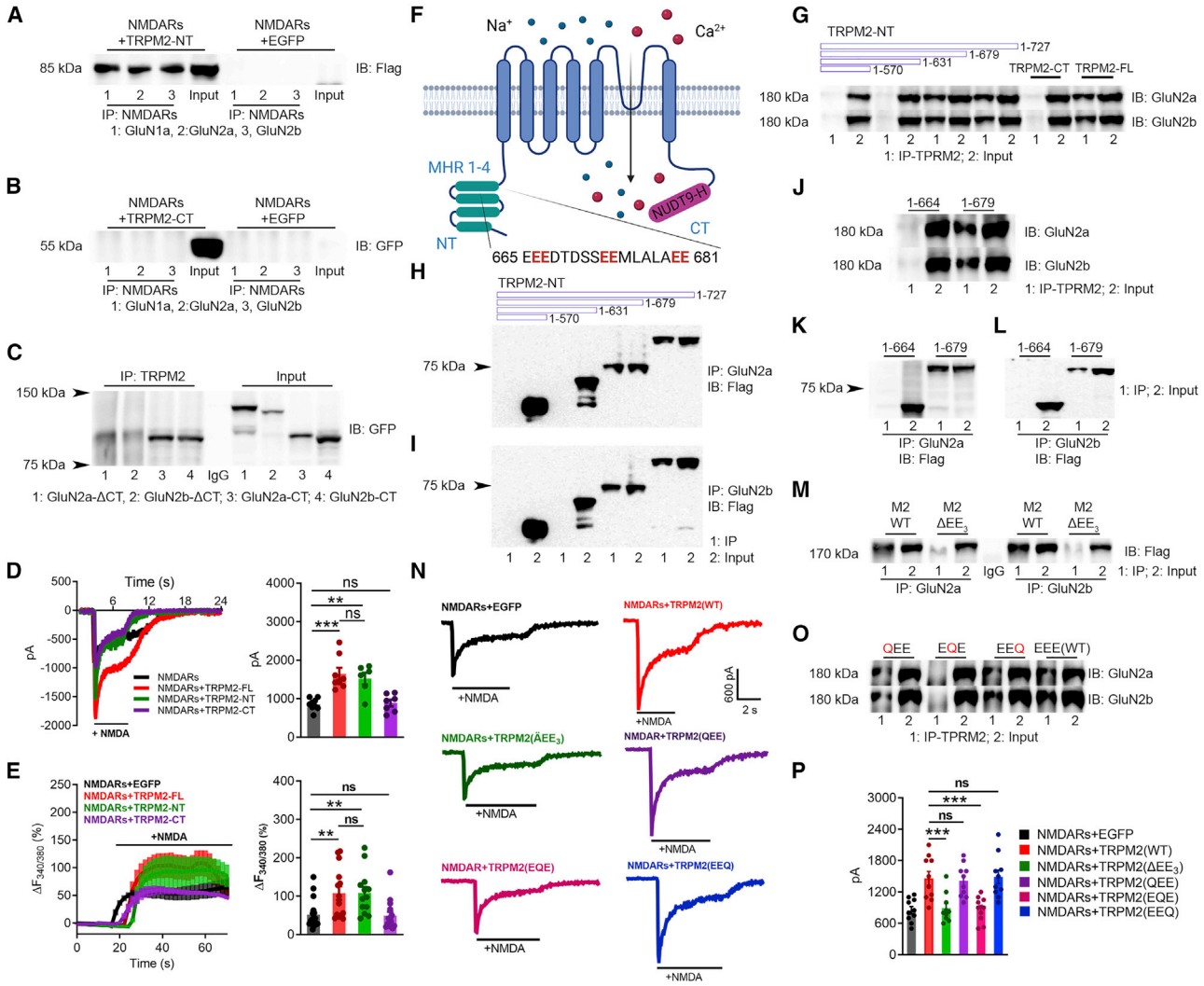

Figure 3. EE_3 motif in TRPM2 mediates TRPM2-NMDARs coupling

(A and B) CoIP of N-terminal and C-terminal fragments of TRPM2 (TRPM2-NT [FLAG-tagged, ~85 kDa], TRPM2-CT [GFP tagged, ~60 kDa]) with NMDARs. (A) IP using anti-NMDARs and IB with anti-Flag. (B) IP using anti-NMDARs and IB using anti-GFP.

(C) CoIP of TRPM2 with the C terminus of GluN2a (GluN2a-CT, 1,054–1,068), C terminus-deleted GluN2a (GluN2a-ΔC, 1–1,053), C terminus of GluN2b (GluN2b-CT, 1,041–1,691), and C-terminus deleted GluN2b (GluN2b-ΔC, 1–1,047). All the constructs were GFP tagged. IP using anti-TRPM2 and IB using anti-GFP.

(D) NMDAR current recording in HEK-293T cells transfected with NMDARs and EGFP, TRPM2-full length (FL), TRPM2-NT, or TRPM2-CT (left). Average current amplitudes (n = 9, 8, 8, 8, respectively).

(E) NMDARs-mediated Ca^{2+} influx in HEK-293T cells transfected with NMDARs and EGFP, TRPM2-full length (FL), TRPM2-NT, or TRPM2-CT (left). Averaged changes of $F_{340/380}$.

(F) Membrane topology of TRPM2. The EE_3 motif is located in the MHR4.

(G–I) CoIP of FLAG-tagged TRPM2 N-terminal segments with different lengths (1–570, 1–631, 1–678, and 1–727) with NMDARs. (G) IP using anti-TRPM2 (anti-GFP for TRPM2-CT) and IB using anti-GluN2a/2b. (H and I) IP using anti-GluN2a (H) or anti-GluN2b (I) and IB using anti-Flag.

(J–L) CoIP of the TRPM2 N-tail fragments (1–664 and 1–679) with NMDARs. (J) IP using anti-TRPM2 and IB using anti-GluN2a/2b. (K and L) IP using anti-GluN2a (K) or anti-GluN2b (L) and IB using anti-Flag.

(M–P), Physical and functional coupling of TRPM2 and NMDARs through EE_3 motif. (M and O) EE_3 motif deletion mutant of TRPM2 (TRPM2-ΔEE_3), and EE_3 mutations of TRPM2, TRPM2-QEE (E666Q, E667Q), TRPM2-EQE (E673Q, E674Q), and TRPM2-EEQ (E680Q, E681Q) were coexpressed with NMDARs in HEK293T cells for coIP. (M) IP using anti-GluN2a/b, and IB using anti-Flag. (O) IP using anti-TRPM2 and IB using anti-GluN2a/2b. (N) NMDAR current recording in HEK293T cells co-expressed with EGFP, WT-TRPM2, TRPM2-ΔEE_3, TRPM2-QEE, TRPM2-EQE, and TRPM2-EEQ. (P) Mean current amplitude (n = 10/group). ns, no statistical significance, **p < 0.01, ***p < 0.001; ANOVA, Bonferroni's test; mean ± SEM.

The C-tails of GluN2a and GluN2b have diverged substantially in evolution. As the EE_3 motif in TRPM2 is largely negatively charged (Figures S4A and S4B), we focused on a segment of GluN2a/GluN2b regions (GluN2a:1,254–1,270; GluN2b: 1,259–1,274; Figure 4C) with positive charges by lysine (K) and arginine (R), which is near the binding site for CaMKII (Bayer et al., 2001;

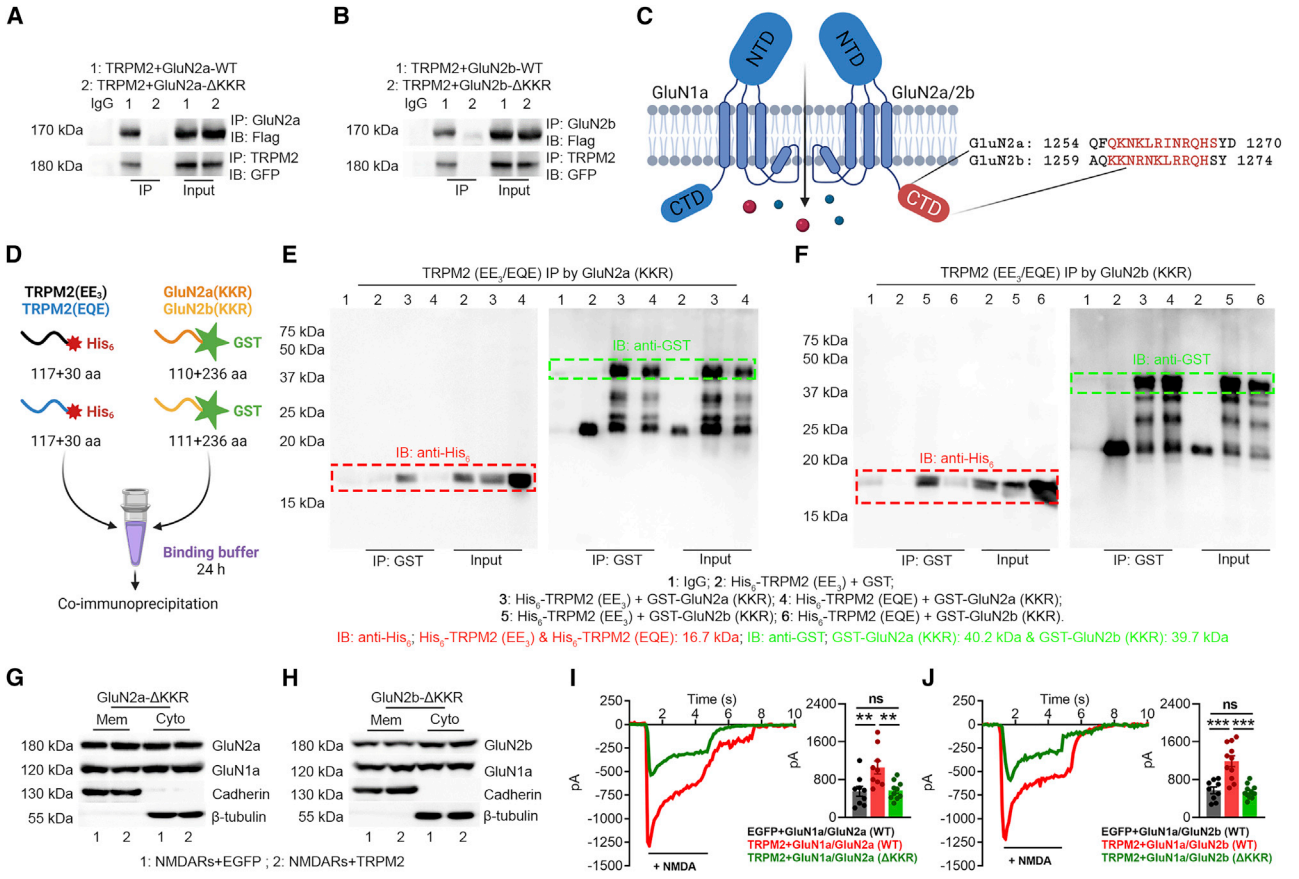

Figure 4. KKR motif in GluN2a and GluN2b is required for the direct binding to the EE_3 motif in TRPM2

(A and B) CoIP of KKR motif deleted GluN2a (GluN2a-ΔKKR, A) and GluN2b (GluN2b-ΔKKR, B) with TRPM2. TRPM2 is FLAG-tagged and GluN2a/GluN2b is GFP tagged. IP using anti-GluN2a/b and IB with anti-Flag (upper). IP using anti-TRPM2 and IB using anti-GFP (lower).

(C) Structure of GluN2a and GluN2b. The KKR motif (red label indicates the deleted sequence [ΔKKR]) is localized within the C-terminal domain (CTD).

(D) Schematic diagram of the *in vitro* binding assay. EE_3 and EQE containing fragments were labeled by a N-terminal His_6 tag and KKR-containing fragments were labeled by a N-terminal GST tag.

(E and F) CoIP of EE_3 and EQE containing fragments with KKR-containing fragments from GluN2a (E) and GluN2b (F). IP using anti-GST and IB using anti-His_6.

(G and H) Surface expression of NMDARs in HEK-293T cells cotransfected with TRPM2 and GluN2a-ΔKKR (G) and GluN2b-ΔKKR (H).

(I and J) NMDAR current recording in HEK-293T cells cotransfected with TRPM2 and GluN2a-ΔKKR (I) and GluN2b-ΔKKR (J).

**p < 0.01; ***p < 0.001; ANOVA, Bonferroni's test; mean ± SEM.

Goodell et al., 2017). We designated this region the "KKR" motif (Figure S4I). The KKR motif is highly conserved between GluN2a and GluN2b and in different species (Figures S4J and S4K). Deletion of KKR motif abolished the interaction between TRPM2 and GluN2a/GluN2b (Figures 4A and 4B), indicating that KRR motif is required for the TRPM2-NMDAR interaction.

We next sought to determine whether EE_3 and KKR motifs directly bind to each other. A 117-residue TRPM2 segment containing either the EE_3 or EQE motif was subcloned into a modified His_6-tag vector (Li and Hao, 2010) (Figures 4D, S5A, and S5B), and the KKR-containing fragments in GluN2a (110 residues) and GluN2b (111 residues) were subcloned into a modified GST-tag vector (Li and Hao, 2010) for expression and purification (Figure S5C). *In vitro* coIP binding assays were performed (Figure 4D). EE_3 motif was coimmunoprecipitated by KKR motifs derived from GluN2a/2b, but EQE was not (Figures 4E, 4F, and S5D). Similarly, KKR motifs were effectively coimmunoprecipitated by EE_3 motif, but not by EQE motif (Figure S5E). These results indicate that TRPM2-GluN2a/GluN2b association is mediated by direct interaction between their EE_3 and KKR motifs, respectively. Moreover, deletion of KKR motif abolished the increased surface expression of NMDAR (Figures 4G, 4H, S5F, and S5G) and the enhanced NMDAR currents (Figures 4I and 4J) induced by TRPM2, confirming the importance of KKR motif in the functional coupling of TRPM2-NMDARs.

Mechanisms of TRPM2-NMDAR functional coupling

Next, we investigated how TRPM2 potentiates NMDAR currents. PKC regulates NMDARs' surface trafficking (Lan et al., 2001; Zheng et al., 1999). PKCγ, the neuron-specific PKC, can be readily coimmunoprecipitated by anti-TRPM2 in the brain lysates (Figure 5A). We further narrowed down that the binding area for PKC on TRPM2 is located on its N-tail using HEK293 cells cotransfected with PKCγ and TRPM2-FL, TRPM2-CT, or

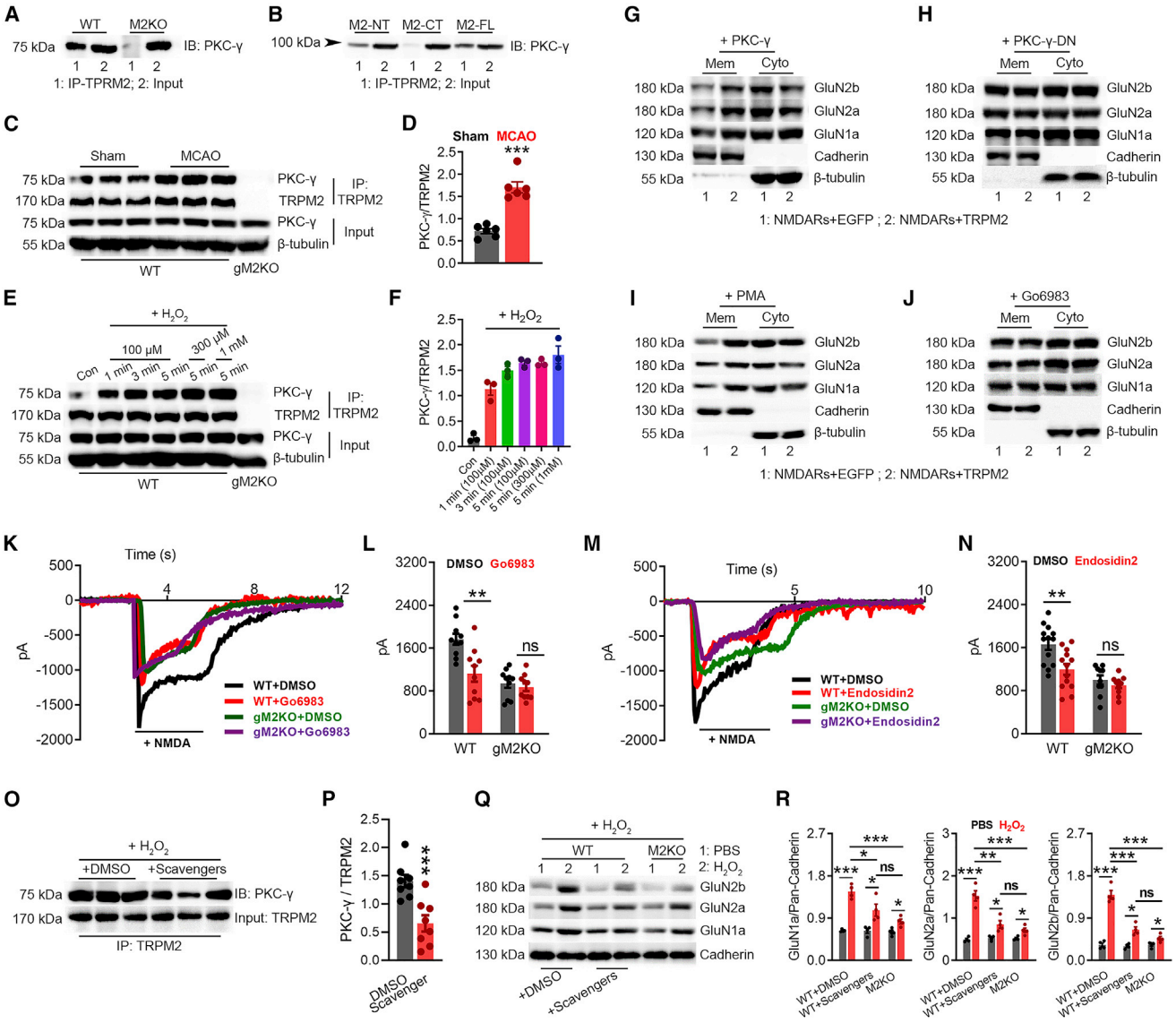

Figure 5. N-tail of TRPM2 Interacts with PKC-γ

(A and B) CoIP of PKCγ and TRPM2 using brain lysates (A) and in HEK293T cells expressing PKCγ with TRPM2-FL, TRPM2-NT, or TRPM2-CT (B). IP using anti-TRPM2 (anti-TRPM2-NT for M2-NT and anti-TRPM2-CT for M2-CT) and IB using anti-PKCγ.

(C and D) CoIP of TRPM2 and PKCγ using brain lysates from WT mice subjected to MCAO or sham surgery. IP using anti-TRPM2 and IB using anti-PKCγ. (D) Quantification of PKCγ/TRPM2 (n = 6/group).

(E and F) CoIP of TRPM2 and PKCγ using neuron lysates from WT mice subjected to H_2O_2 treatment (at 100 μM for 1, 3, and 5 min, at 300 μM for 5 min and at 1 mM for 5 min). (E) IP using anti-TRPM2 and IB using anti-PKCγ. (F) Quantification of PKCγ/TRPM2 (n = 3/group).

(G and H) Surface expression of NMDARs in HEK-293T cells cotransfected with PKC-γ/EGFP and PKC-γ/TRPM2 (G) or PKC-γ-DN/EGFP and PKC-γ-DN/TRPM2 (H).

(I and J) Surface expression of NMDARs in HEK-293T cells cotransfected with TRPM2 or EGFP with the treatment of PKC activator PMA (I) or inhibitor Go6893 (J).

(K and L) NMDAR current recording in WT and gM2KO neurons treated with or without Go6983 at 1 μM for overnight. (L) Mean current amplitude (n = 10–15 neurons from 2 mice).

(M and N) NMDAR current recording in WT and gM2KO neurons treated with or without the treatment of exocytosis inhibitor endosidin 2 at 1 μM overnight. (N) Mean current amplitude (n = 10–15 neurons from 2 mice).

(O and P) CoIP of TRPM2 and PKCγ using neuron lysates from WT mice subjected to H_2O_2 treatment at 100 μM for 3 min with the preincubation of DMSO or scavengers. (P) CoIP using anti-TRPM2 and IB using anti-PKCγ. (D) Quantification of PKCγ/TRPM2 (n = 6/group).

(Q and R) Surface expression of NMDARs in isolated WT neurons subjected to H_2O_2 at 100 μM for 3 min with the preincubation of DMSO or scavengers (n = 4 in each group).

ns, no statistical significance, *p < 0.05, **p < 0.01, ***p < 0.001; ANOVA, Bonferroni's test; mean ± SEM.

TRPM2-NT (Figure 5B). Moreover, MCAO increased the binding of PKCγ to TRPM2 in the brain (Figures 5C and 5D). Similarly, cultured neurons treated with H_2O_2 exhibited markedly increased TRPM2-PKCγ interaction (Figures 5E and 5F).

To determine whether TRPM2-PKCγ association influences the surface expression of NMDARs, NMDARs/TRPM2 were coexpressed with WT PKCγ or dominant-negative PKCγ (PKCγ-DN) (Colgan et al., 2018; Soh and Weinstein, 2003) (Figures 5G, 5H, S6A, and S6B). Overexpression of PKCγ further increased the TRPM2-induced increase of NMDARs' surface expression, whereas PKCγ-DN abolished this increase, suggesting that a functional PKCγ is required for TRPM2-mediated increase of NMDARs' surface expression. Indeed, PKC activator PMA also markedly increased the TRPM2-induced increase of NMDARs' surface expression (Figures 5I, S6C, and S6E), whereas PKC inhibitors Go6983 and staurosporine abolished this increase (Figures 5J, S6D, S6F, and S6G). Similarly, Go6983 and staurosporine reduced the NMDAR current amplitude in WT neurons to a similar level as in gM2KO neurons (Figures 5K, 5L, S6H, and S6I).

Surface trafficking of NMDARs involves exocysts (Sans et al., 2003). Endosidin 2, an exocyst inhibitor, prevented the increased surface expression of NMDARs induced by TRPM2 (Figures S6J and S6K). Also, endosidin 2 pretreatment inhibited NMDAR currents in WT neurons, but not in gM2KO neurons (Figures 5M and 5N). CaMKII is known to be important in NMDAR trafficking. CaMKII inhibitor KN93 inhibited the increased surface expression of NMDARs (Figures S6L and S6M) induced by TRPM2 and reduced NMDAR current amplitude in WT neurons to the similar level in gM2KO neurons (Figures S6N and S6O). Preincubation with oxidative stress scavengers Mn(III)TBAP together with L-NMA inhibited the H_2O_2-induced binding of PKCγ to TRPM2 (Figures 5O and 5P). Moreover, the enhanced surface expression of NMDARs induced by H_2O_2 in WT neurons was reduced by scavengers to the similar levels as that in M2KO neurons (Figures 5Q and 5R).

Taken together, the above results indicate that PKCγ interacts with TRPM2, which can be promoted by oxidative stress *in vitro* and by MCAO *in vivo*, and suggest that the TRPM2-PKCγ association may be required for the functional coupling between TRPM2 and NMDAR.

TAT-EE_3 eliminates TRPM2-NMDAR coupling

As the TRPM2 N-terminal EE_3 motif is critical for the TRPM2-NMDAR interaction, we designed a membrane-permeable interfering peptide, TAT-EE_3, and scrambled control TAT-SC or TAT-EQE to investigate whether disruption of the physical interaction influences their functional coupling. Similar to TRPM2-$\Delta(EE)_3$ and TRPM2-EQE mutants, TAT-EE_3 treatment completely disrupted the interaction of TRPM2 with GluN2a (Figure 6A) and GluN2b (Figure 6B). Also, the enhancement of NMDARs' surface expression (Figures 6C, 6D, S6P, and S6Q) and the increase of NMDAR current amplitude (Figures 6E and 6F) induced by TRPM2 were inhibited by TAT-EE_3.

PKC can increase both the surface trafficking and channel activity of NMDARs (Lan et al., 2001). In WT neurons treated with TAT-SC, NMDAR-induced current was increased from 1,542.1 ± 117.1 pA to 3,642.1 ± 180.8 pA by a 20-s PMA perfusion (Figure 6G, top left), which is about a 1.5-fold increase (Figures 6H and 6I). However, in WT neurons treated with TAT-EE_3, NMDAR currents were substantially reduced before and after PMA perfusion (Figure 6G, top right), and the current potentiation by PMA was also eliminated (Figures 6H and 6I). In neurons from gM2KO mice, the basal NMDAR current amplitude (Figure 6G, bottom) and PMA-induced increase were much smaller than that of WT neurons, and TAT-EE_3 did not cause additional inhibition (Figures 6H and 6I). These data further support our hypothesis that the TRPM2-PKCγ association is required for the functional coupling between TRPM2 and NMDAR.

Disruption of TRPM2-NMDAR interaction protects neurons against OGD

The functional uncoupling of TRPM2 from NMDARs by TAT-EE_3 prompted us to investigate its potential protective effect against ischemic injury. Pretreatment of TAT-EE_3 inhibited the NMDAR currents in WT neurons, but not in M2KO neurons (Figures 7A and 7B), indicating the specificity of TAT-EE_3 in disrupting the TRPM2-NMDAR interaction. When neurons were exposed to OGD, the increase of intracellular Ca^{2+} was markedly inhibited in WT, but not in gM2KO neurons pretreated with TAT-EE_3 (Figures 7C and 7D). Moreover, OGD-mediated neuronal deaths in WT neurons treated with TAT-SC were 10.6%, 47.6%, and 70.5% at 30, 60, and 90 min, respectively, which were drastically reduced by TAT-EE_3 to 3.6%, 9.9%, and 45.2%, similar to the levels of those in M2KO neurons (Figure 7E). Moreover, TAT-EE3 inhibited OGD-induced mitochondria depolarization in WT neurons to the similar levels as those in neurons from gM2KO or nM2KO mice (Figures 7G and 7H). The observed mitochondrial dysfunction was supposed to be mediated by Ca^{2+} entry, as mitochondria depolarization was inhibited when neurons were perfused with Ca^{2+}-free OGD solution (last column in Figure 7G, micrographs, and Figure 7H). In summary, TAT-EE_3 inhibited the exacerbation of excitotoxicity caused by TRPM2-NMDAR coupling and protects neuron against OGD.

Uncoupling of TRPM2-NMDAR association attenuates ischemic stroke

We first determined the efficacy of TAT-EE_3 in disrupting the TRPM2-NMDAR interaction *in vivo*. TAT-EE_3, TAT-SC, and TAT-EQE were intraperitoneally (i.p.) administrated to WT mice prior to MCAO surgery, and the TRPM2-NMDAR interaction was assessed by coIP at 2, 12, and 24 h after i.p. injection. TAT-EE_3 effectively disrupted the TRPM2-NMDAR interaction at 2 and 12 h, whereas at 24 h, there was an ~40% recovery of TRPM2-NMDAR interaction. In contrast, the sequence-specific scramble TAT-EQE did not influence the interaction, similar to that of the random scramble TAT-SC (Figure 8A). We then designed an i.p. injection strategy (Figure 8B). TAT-EE_3, TAT-EQE, or TAT-SC was i.p. administrated before MCAO (pre-MCAO) or after MCAO (post-MCAO), followed by reinjection every 12 h till the time for infarction assessment. For pre-MCAO treatment, TAT-EE_3 or TAT-SC (100 nmol/kg, estimated to be 2 μM based on 1 mL blood) were i.p. administrated 15 min before MCAO or sham surgery as previously reported (Weilinger et al., 2016).

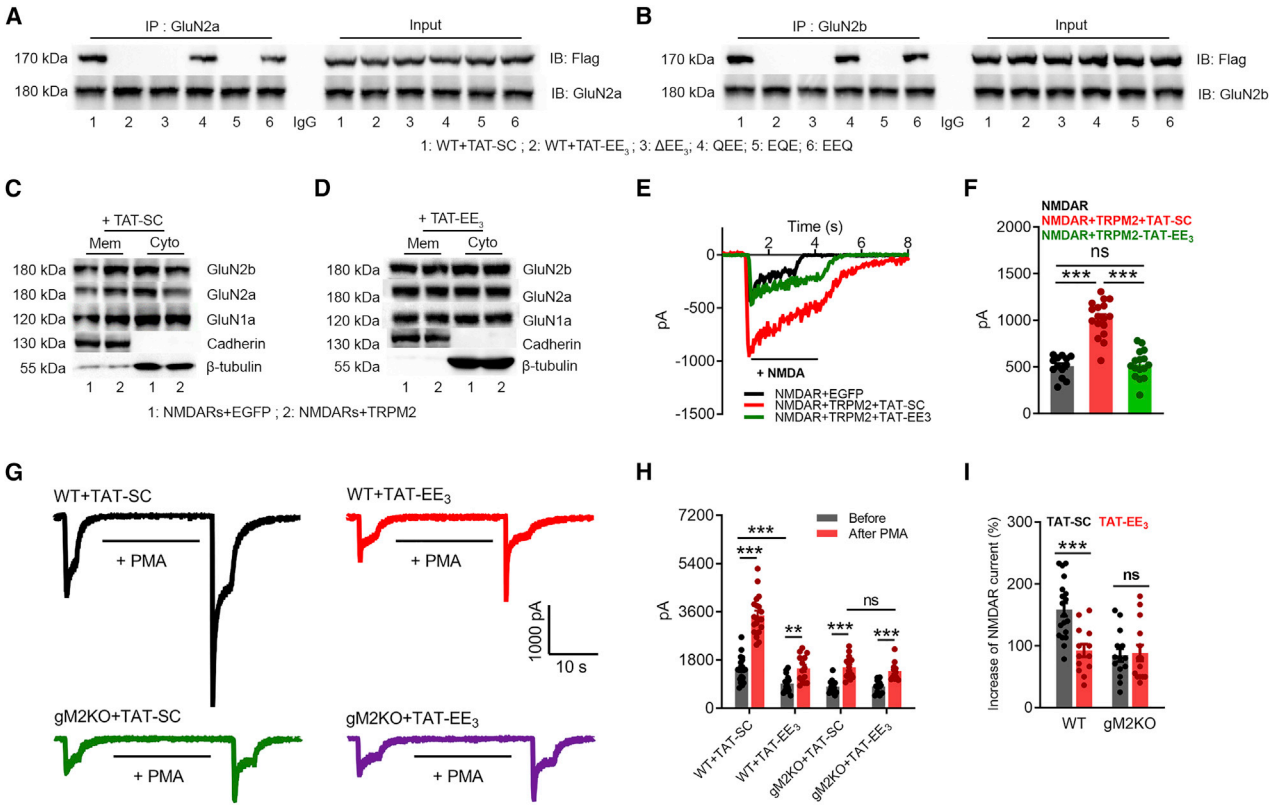

Figure 6. TAT-EE$_3$ disrupts the physical and functional interaction between TRPM2 and NMDAR

(A and B) CoIP of NMDARs with WT or EE$_3$-domain mutants of TRPM2 (FLAG-tagged). IP using anti-GluN2a (A) or anti-GluN2b (B), and IB using anti-Flag.

(C and D) Surface expression of NMDARs in HEK-293T cells cotransfected with TRPM2 or EGFP with the treatment of 10 μM TAT-SC (C) or TAT-EE$_3$ (D) overnight.

(E and F) NMDAR current recording in HEK293T cells cotransfected with TRPM2 and NMDARs and treated with 10 μM TAT-EE$_3$ or TAT-SC for overnight. (F) Mean current amplitude (n = 13, 16, 17, respectively).

(G and I) Effects of TAT-EE$_3$ on PKC-induced changes of NMDAR currents recorded in WT and gM2KO neurons. Neurons were pre-incubated with 10 μM TAT-SC or TAT-EE$_3$ overnight. (G) NMDAR current recording in WT and gM2KO neurons before and after PMA (1 μM) perfusion for 20 s. (H) Average current amplitude. (I) Average percentage increases of NMDAR currents induced by PMA (n = 10–15/group).

ns, $p > 0.05$; **$p < 0.01$; ***$p < 0.001$; ANOVA, Bonferroni's test; mean ± SEM.

TAT-EE$_3$-treated mice exhibited reduced infarct volume and improved neurological deficit (ND) score (Figures 8C–8E). For the post-MCAO treatment, we evaluated the protective effects of TAT-EE$_3$ at 24 h, 3 days, and 7 days. As shown in Figures 8C–8E, post-MCAO TAT-EE$_3$ treatment reduced infarct volume and improved ND score in WT mice but did not produce further protective effects in the nM2KO mice, indicating that TAT-EE$_3$ specifically targets TRPM2. For the long-term MCAO (7 days), we evaluated ND score as well as behavioral changes using rotarod test at day 1, day 3, and day 7. TAT-EE$_3$ improved ND scores at day 1, day 3, and day 7 (Figure 8F) and inhibited the reduction of "latency to fall" time (Figure 8G). Moreover, the MCAO-induced increase of the surface expression of NMDARs was markedly inhibited by TAT-EE$_3$ to a similar level as that in gM2KO and nM2KO (Figures 8H and 8I). These results suggest that TAT-EE$_3$ disrupts TRPM2-NMDAR coupling (Figure 8A) and reduces surface expression of NMDARs (Figure 8H), thereby protecting mice against ischemic stroke.

Synaptic NMDARs (sNMDARs) promote while extrasynaptic NMDAR (esNMDARs) inhibit neuron survival (Figure S7A). sNMDARs and esNMDARs can be selectively activated based on a well-established protocol (Hardingham et al., 2002; Nicolai et al., 2010). As shown in Figures 8J and 8K, activation of esNMDARs by NMDA inhibited the activation of the prosurvival ERK1/2 (pERK1/2) and CREK (pCREB), whereas activation of sNMDARs by 4-AP/Bic increased the phosphorylation of ERK1/2 and CREB. In contrast, TAT-EE$_3$ treatment markedly reduced the inhibition of NMDA on pERK1/2 and pCREB (Figures 8J and 8K). Similarly, inhibition of pERK1/2 and pCREB in the brain by MCAO were prevented by TAT-EE$_3$ to a similar level as that in nM2KO (Figures 8L and 8M) and gM2KO (Figure S7B).

The preferential effects of TRPM2 on esNMDARs are consistent with the observation that TRPM2 is absent in the synaptome databases (Bayés et al., 2012; Yan et al., 2020). We also found that TRPM2 was not present in the coimmunoprecipitate by anti-PSD95, a synaptic protein associating with sNMDARs (Figure 8N). Moreover, TRPM2 was barely detected in isolated synaptosomes from the brain (Figure 8O). We also isolated the esNMDAR-mediated Ca^{2+} response (Bengtson et al., 2008;

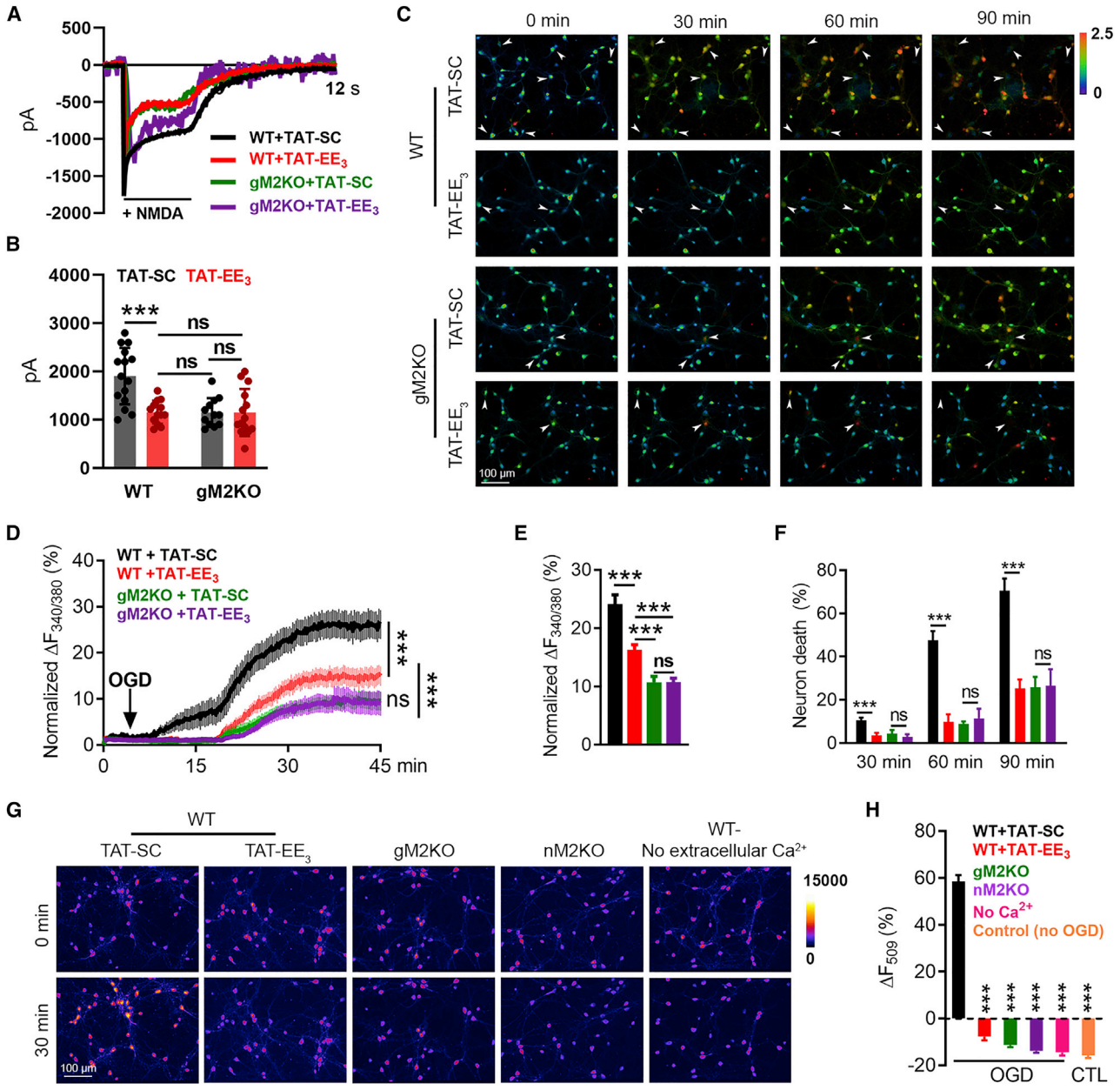

Figure 7. Uncoupling TRPM2 and NMDARs by TAT-EE$_3$ protects neurons against OGD-induced injury

(A and B) NMDAR current recording in WT and global TRPM2 knockout (gM2KO) neurons treated with 10 μM TAT-EE$_3$ or TAT-SC for overnight. (B) Mean current amplitude (n = 15, 13, 12, and 14, respectively).

(C–F), Ratio Ca^{2+} imaging. (C) Arrows indicate representative lysed neurons with increasing intracellular Ca^{2+}. (D) Averaged Ca^{2+} imaging traces (n = 20/group). (E) Quantification of OGD-induced Fura-2 fluorescence changes (n = 179, 269, 232, 242/4 dishes, respectively). (F) OGD-induced neuronal death (n = 4/group).

(G and H) R123 imaging. (G) R123-labeled mitochondria before and 30 min after OGD. (H) Quantification of R123 change (n = 296, 262, 265, 208, 145, 258/4 dishes, respectively).

***p < 0.001; ANOVA, Bonferroni's test; mean ± SEM.

Hardingham et al., 2002) and found that the esNMDAR-mediated increase of intracellular Ca^{2+} was inhibited by *Trpm2* deletion, whereas the sNMDAR-mediated Ca^{2+} response was not altered. These results suggest that TRPM2 is located at the extrasynaptic sites and preferentially enhances esNMDAR-mediated Ca^{2+} signals.

DISCUSSION

In this study, we revealed a potential therapeutic strategy for ischemic stroke by targeting TRPM2-NMDAR association. Previous studies have shown the protective effects of global *Trpm2* deletion (Alim et al., 2013; Belrose and Jackson, 2018; Gelderblom

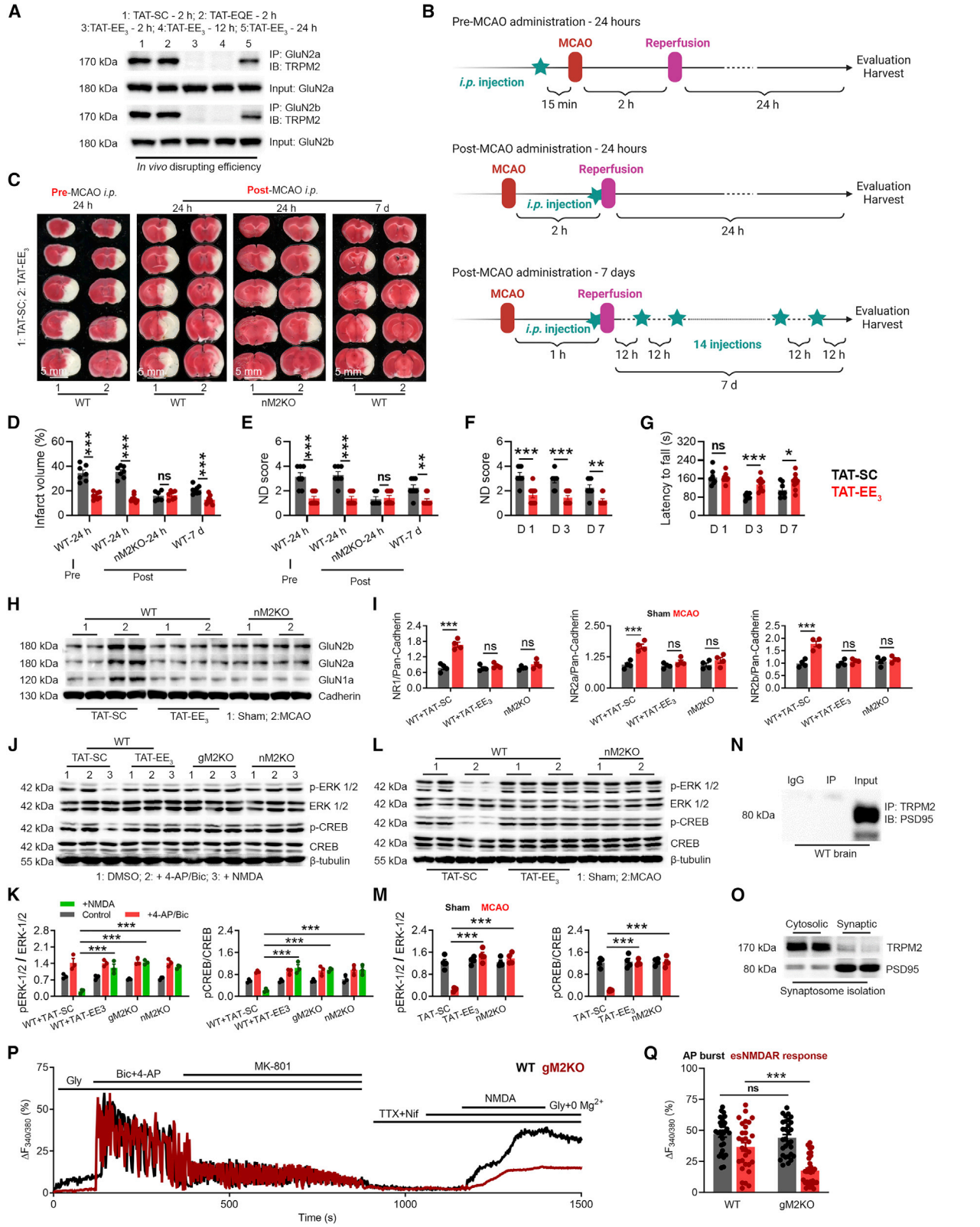

(legend on next page)

et al., 2014; Mai et al., 2020). Our neuron-specific *Trpm2* deletion results establish that neuronal TRPM2 plays a key role in aggregating excitotoxic neuronal apoptosis and necrosis in ischemic stroke through a previously unknown mechanism: physical and functional coupling with NMDARs. TRPM2 directly interact with GluN2a/b through the unique EE_3 motif in its N-tail and the KKR motifs in the C-tail of GluN2a/b. The EE3 motif is evolutionally conserved in TRPM2 of different species but absent in other subfamilies of TRP channels, including TRPM4, which was shown to interact with GluN2a/2b (Yan et al., 2020).

We showed that TRPM2 selectively enhances the activity of esNMDARs by increasing surface expression, which is mediated by recruitment of PKCγ to the TRPM2-NMDAR complex. PKC regulates NMDAR's surface trafficking via different mechanisms. Some studies demonstrated that PKC phosphorylates serine residues (Ser896 and Ser897) on GluN1 (Horak and Wenthold, 2009; Scott et al., 2001; Standley et al., 2000), whereas others showed the regulation of PKC on NMDARs is not mediated by directly phosphorylation (Zheng et al., 1999) but by triggering autophosphorylation of CaMKII that associates with NMDARs (Yan et al., 2011). Interestingly, CaMKII inhibitor can reduce the enhanced surface expression of NMDARs in our study. Moreover, we found that TRPM2-induced increase of NMDARs' surface expression can be inhibited by the exocyst inhibitor endosidin 2 (Sans et al., 2003; Zhang et al., 2016). NMDARs have been shown to interact with the exocyst (Sans et al., 2003) for PKC-induced surface trafficking. Although we do not know the exact mechanism by which PKCγ mediates trafficking of the TRPM2-NMDAR complex, we propose the following working model. Under oxidative stress conditions, TRPM2 recruits PKCγ to the TRPM2/NMDARs to bring PKCγ to the close proximity of NMDAR-interacting partners such as CaMKII and consequently promotes NMDARs' surface trafficking, leading to enhanced excitotoxicity. Nonetheless, future investigations are needed to understand where PKCγ begins to bind to the TRPM2-NMDAR complex.

We found that TRPM2 exacerbates excitotoxicity by preferentially enhancing the function of esNMDARs. Disruption of TRPM2-NMDAR interaction by TAT-EE_3 prevented the inhibition on phosphorylation of ERK1/2 and CREB, the prosurvival signaling that can be shut off by esNMDAR activation during ischemic stroke (Hardingham and Bading, 2010; Hardingham et al., 2002), indicating that disruption of TRPM2-NMDAR coupling largely eliminates the esNMDAR-mediated excitotoxicity. It is not surprising that TRPM2 preferentially influence esNMDARs because we found that TRPM2 could not be detected in the synaptosomes or immunoprecipitated by anti-PSD-95. Moreover, *Trpm2* deletion significantly reduced extrasynaptic, but not the synaptic, NMDA-induced Ca^{2+} response. Similarly, other studies have demonstrated a predominantly extrasynaptic distribution of TRPM2 in cultured hippocampal neurons (Olah et al., 2009) and that TRPM2 is absent in the synaptic proteins (Bayés et al., 2012). Importantly, TRPM2 only enhances NMDAR function during ischemic stroke, as TRPM2-NMDAR interaction and increase of NMDARs' surface trafficking are promoted by PKCγ under oxidative stress conditions. Thus, disrupting the TRPM2-NMDAR interaction to specifically target esNMDARs will unlikely generate similar side effects caused by inhibition of synaptic NMDARs by conventional NMDAR antagonists.

The most exciting result in our study is that the TRPM2-derived interfering peptide TAT-EE_3 protects mice against ischemic stroke in both short- and long-term MCAO. Cell-permeable peptides such as TAT-fused peptides have been well characterized and are considered powerful tools for both clinical applications and basic research studies (Xie et al., 2020). We found that TAT-EE3 disrupts TRPM2-NMDAR interaction *in vitro* and *in vivo*, effectively inhibits excitotoxicity, and prevents the reduction of phosphorylated CREB and ERK1/2 levels. Our results indicate that peptide-based uncoupling of TRPM2-NMDAR association is a promising therapeutic strategy for ischemic stroke.

NMDARs interact with various proteins (Petit-Pedrol and Groc, 2021). A recent study showed that interaction of GluN2a/b with the Ca^{2+}-impermeable channel TRPM4 through a 57-aa domain (TwinF) in the N-tail of TRPM4 enhances excitotoxicity (Yan et al., 2020). Interestingly, interaction of TRPM4 with NMDARs does not influence NDMAR currents or Ca^{2+} signaling but promotes prodeath signaling. The authors demonstrated that the physical coupling of TRPM4 and NMDARs is required to promote excitotoxicity (Yan et al., 2020). Similar to TRPM2, TRPM4 preferentially influences esNMDARs. It would be exciting to speculate that like scaffolding proteins for synaptic NMDARs' trafficking,

Figure 8. TAT-EE_3 alleviates ischemic stroke by preserving prosurvival signaling

(A) CoIP of TRPM2 and GluN2a/2b in the brain lysates from WT mice after MCAO with the treatment of TAT-SC for 2 h, TAT-EQE for 2 h, and TAT-EE_3 for 2, 12, and 24 h. IP using anti-GluN2a/2b and IB using anti-TRPM2.

(B) Graphic illustration of injection strategy. For pre-MCAO administration, TAT-EE_3 was injected intraperitoneally (i.p.) 30 min before the MCAO. For post-MCAO administration, TAT-EE_3 was injected right before the reopening of the occulated MCA to best mimic the treatment of ischemic stroke under clinical situation. For examining the long-term protective effects, mice were subjected to a 1 h MCAO, and TAT-EE_3 was administered every 12 h based on the pre-evaluated *in vivo* disrupting efficacy (Figure 8A).

(C–G) TAT-EE_3 protects WT mice against MCAO. (C) TTC staining of brain slices. (D) Mean infarct volume. (E) Average neurological deficit (ND) score. Average ND score (F) and average latency to fall time (G) for the long-term MCAO experiment (neuron-specific TRPM2 knockout [nM2KO]).

(H and I) WB analysis of the surface expression of NMDARs in the brain (n = 4/group).

(J and K) WB of ERK1/2 and CREB phosphorylation in cultured neurons isolated from global TRPM2 knockout (gM2KO) and nM2KO mice and WT littermates. WT neurons were pretreated with TAT-EE_3 or TAT-SC overnight (n = 3/group).

(L and M) WB of ERK1/2 and CREB phosphorylation in the brains from WT and nM2KO mice subjected to MCAO (n = 4/group).

(N) IP using anti-PSD-95 and IB using anti-TRPM2.

(O) WB of TRPM2 expression in synaptosomes.

(P and Q) Isolation of extrasynaptic NMDAR-mediated Ca^{2+} response in WT and gM2KO neurons. (P) Representative Ca^{2+} imaging traces (Q) Quantification of AP burst (synaptic NMDAR-mediated response) induced by 4-AP/Bic, and extrasynaptic NMDAR-mediated response by NDMA (n = 30/group).

ns, no statistical significance, *p < 0.05, **p < 0.01, ***p < 0.001; ANOVA, Bonferroni's test; mean ± SEM.

TRPM2 and TRPM4 may represent a family of proteins that are able to form interacting complex with NMDARs and may exclusively localize NMDARs to the extrasynaptic sites. Moreover, as shown by previous studies that GluN2b is preferentially localized at extrasynaptic sites (Ge et al., 2020), it will be of a great interest to understand how TRPM2 in our study and TRPM4 in the previous study (Yan et al., 2020) only influence esNMDARs but interact with both GluN2a and GluN2b.

In summary, we found that TRPM2 in neurons promotes neuronal death during ischemic stroke by coupling with esNMDARs via its EE_3 motif. Targeting TRPM2-NMDAR interaction could be a promising strategy for developing more effective and safer therapies for ischemic stroke.

STAR★METHODS

Detailed methods are provided in the online version of this paper and include the following:

- KEY RESOURCES TABLE
- RESOURCE AVAILABILITY
  - Lead contact
  - Material availability
  - Data and code availability
- EXPERIMENTAL MODEL AND SUBJECT DETAILS
  - Animals
  - Cortical neuron isolation and culture
  - Cell line culture and transfection
- METHOD DETAILS
  - Middle cerebral artery occlusion (MCAO)
  - Neurological deficit score evaluation
  - Rotarod test
  - Infarct volume assessment by Triphenyl Tetrazolium chloride (TTC) staining
  - Antibodies, chemicals, and reagents
  - Membrane permeable peptide TAT-EE_3 for disrupting TRPM2 and NMDARs coupling and scramble control TAT-SC peptides
  - Plasmids and enzymes
  - Subcloning
  - *E. coli* expression and purification of proteins
  - *In vitro* protein-protein direct binding assay
  - Oxygen-glucose deprivation
  - Ratio calcium imaging experiments
  - Co-immunoprecipitation
  - Western blotting
  - Electrophysiology
  - Immunofluorescence staining
- QUANTIFICATION AND STATISTICAL ANALYSIS

SUPPLEMENTAL INFORMATION

Supplemental information can be found online at https://doi.org/10.1016/j.neuron.2022.03.021.

ACKNOWLEDGMENTS

We would like to thank Drs. Rajkumar Verma (UConn Health) and Louise McCullough (UT Health) for constructive discussions about this project. We thank Drs. Rindy Jaffe and Dejian Ren for helpful comments to the manuscript. We thank Dr. Andrew M. Scharenberg (University of Washington) for kindly providing TRPM2 plasmid. This work was partially supported by the National Institutes of Health (R01-HL143750) and American Heart Association (19TPA34890022) to L.Y. and National Institutes of Health (R01-GM135592) to B.H.

AUTHOR CONTRIBUTIONS

L.Y. conceived and designed the research. P.Z. designed and performed most of the *in vitro* experiments. Z.Y. and J.F. performed most of the *in vivo* experiments. Z.Y., B.S., Y.H., Z.S., A.S.Y., and J.X. conducted some of the *in vitro* experiments. G.W. conducted MCAO surgeries and supervised others doing *in vivo* MCAO surgeries. B.H. supervised Y.L. and P.Z. for the direct protein binding experiments. B.M. and Y.M. generated knockout mice and provided input to discussion of the research. P.Z. and J.F. helped in preparation of the manuscript. L.Y. wrote the manuscript and all authors commented on the manuscript.

DECLARATION OF INTERESTS

P.Z., J.F., and L.Y. have a pending UCONN provisional patent for TRPM2-based therapies for stroke, filed: July 2020.

INCLUSION AND DIVERSITY

We worked to ensure sex balance in the selection of non-human subjects. While citing references scientifically relevant for this work, we also actively worked to promote gender balance in our reference list.

Received: July 9, 2021
Revised: February 12, 2022
Accepted: March 14, 2022
Published: April 13, 2022

REFERENCES

Alim, I., Teves, L., Li, R., Mori, Y., and Tymianski, M. (2013). Modulation of NMDAR subunit expression by TRPM2 channels regulates neuronal vulnerability to ischemic cell death. J. Neurosci. *33*, 17264–17277. https://doi.org/10.1523/JNEUROSCI.1729-13.2013.

Bading, H. (2013). Nuclear calcium signalling in the regulation of brain function. Nat. Rev. Neurosci. *14*, 593–608. https://doi.org/10.1038/nrn3531.

Bayer, K.U., De Koninck, P., Leonard, A.S., Hell, J.W., and Schulman, H. (2001). Interaction with the NMDA receptor locks CaMKII in an active conformation. Nature *411*, 801–805. https://doi.org/10.1038/35081080.

Bayés, A., Collins, M.O., Croning, M.D., van de Lagemaat, L.N., Choudhary, J.S., and Grant, S.G. (2012). Comparative study of human and mouse postsynaptic proteomes finds high compositional conservation and abundance differences for key synaptic proteins. PLoS One *7*, e46683. https://doi.org/10.1371/journal.pone.0046683.

Belrose, J.C., and Jackson, M.F. (2018). TRPM2: a candidate therapeutic target for treating neurological diseases. Acta Pharmacol. Sin *39*, 722–732. https://doi.org/10.1038/aps.2018.31.

Belrose, J.C., Xie, Y.F., Gierszewski, L.J., MacDonald, J.F., and Jackson, M.F. (2012). Loss of glutathione homeostasis associated with neuronal senescence facilitates TRPM2 channel activation in cultured hippocampal pyramidal neurons. Mol. Brain *5*, 11. https://doi.org/10.1186/1756-6606-5-11.

Bengtson, C.P., Dick, O., and Bading, H. (2008). A quantitative method to assess extrasynaptic NMDA receptor function in the protective effect of synaptic activity against neurotoxicity. BMC Neurosci. *9*, 11. https://doi.org/10.1186/1471-2202-9-11.

Chiang, T., Messing, R.O., and Chou, W.H. (2011). Mouse model of middle cerebral artery occlusion. J. Vis. Exp. *48*, 2761.

Choi, D.W. (1995). Calcium: still center-stage in hypoxic-ischemic neuronal death. Trends Neurosci. *18*, 58–60.

Choi, D.W. (2020). Excitotoxicity: still hammering the ischemic brain in 2020. Front. Neurosci. *14*, 579953. https://doi.org/10.3389/fnins.2020.579953.

Colgan, L.A., Hu, M., Misler, J.A., Parra-Bueno, P., Moran, C.M., Leitges, M., and Yasuda, R. (2018). PKCα integrates spatiotemporally distinct Ca^{2+} and autocrine BDNF signaling to facilitate synaptic plasticity. Nat. Neurosci. *21*, 1027–1037. https://doi.org/10.1038/s41593-018-0184-3.

Du, J., Xie, J., and Yue, L. (2009a). Intracellular calcium activates TRPM2 and its alternative spliced isoforms. Proc. Natl. Acad. Sci. USA *106*, 7239–7244. https://doi.org/10.1073/pnas.0811725106.

Du, J., Xie, J., and Yue, L. (2009b). Modulation of TRPM2 by acidic pH and the underlying mechanisms for pH sensitivity. J. Gen. Physiol. *134*, 471–488. https://doi.org/10.1085/jgp.200910254.

Du, J., Xie, J., Zhang, Z., Tsujikawa, H., Fusco, D., Silverman, D., Liang, B., and Yue, L. (2010). TRPM7-mediated Ca^{2+} signals confer fibrogenesis in human atrial fibrillation. Circ. Res. *106*, 992–1003. https://doi.org/10.1161/CIRCRESAHA.109.206771.

Fonfria, E., Murdock, P.R., Cusdin, F.S., Benham, C.D., Kelsell, R.E., and McNulty, S. (2006). Tissue distribution profiles of the human TRPM cation channel family. J. Recept. Signal Transduct. Res. *26*, 159–178. https://doi.org/10.1080/10799890600637506.

Ge, Y., Chen, W., Axerio-Cilies, P., and Wang, Y.T. (2020). NMDARs in cell survival and death: implications in stroke pathogenesis and treatment. Trends Mol. Med. *26*, 533–551. https://doi.org/10.1016/j.molmed.2020.03.001.

Gelderblom, M., Melzer, N., Schattling, B., Göb, E., Hicking, G., Arunachalam, P., Bittner, S., Ufer, F., Herrmann, A.M., Bernreuther, C., et al. (2014). Transient receptor potential melastatin subfamily member 2 cation channel regulates detrimental immune cell invasion in ischemic stroke. Stroke *45*, 3395–3402. https://doi.org/10.1161/STROKEAHA.114.005836.

Goldberg, M.P., and Choi, D.W. (1993). Combined oxygen and glucose deprivation in cortical cell culture: calcium-dependent and calcium-independent mechanisms of neuronal injury. J. Neurosci. *13*, 3510–3524.

Goodell, D.J., Zaegel, V., Coultrap, S.J., Hell, J.W., and Bayer, K.U. (2017). DAPK1 mediates LTD by making CaMKII/GluN2B binding LTP specific. Cell Rep. *19*, 2231–2243. https://doi.org/10.1016/j.celrep.2017.05.068.

Granzotto, A., Canzoniero, L.M.T., and Sensi, S.L. (2020). A neurotoxic menage-a-trois: glutamate, calcium, and zinc in the excitotoxic cascade. Front. Mol. Neurosci. *13*, 600089. https://doi.org/10.3389/fnmol.2020.600089.

Hara, Y., Wakamori, M., Ishii, M., Maeno, E., Nishida, M., Yoshida, T., Yamada, H., Shimizu, S., Mori, E., Kudoh, J., et al. (2002). LTRPC2 Ca2+-permeable channel activated by changes in redox status confers susceptibility to cell death. Mol. Cell *9*, 163–173.

Hardingham, G. (2019). NMDA receptor C-terminal signaling in development, plasticity, and disease. F1000Res *8*, 8. https://doi.org/10.12688/f1000research.19925.1.

Hardingham, G.E., and Bading, H. (2010). Synaptic versus extrasynaptic NMDA receptor signalling: implications for neurodegenerative disorders. Nat. Rev. Neurosci. *11*, 682–696. https://doi.org/10.1038/nrn2911.

Hardingham, G.E., Fukunaga, Y., and Bading, H. (2002). Extrasynaptic NMDARs oppose synaptic NMDARs by triggering CREB shut-off and cell death pathways. Nat. Neurosci. *5*, 405–414. https://doi.org/10.1038/nn835.

Horak, M., and Wenthold, R.J. (2009). Different roles of C-terminal cassettes in the trafficking of full-length NR1 subunits to the cell surface. J. Biol. Chem. *284*, 9683–9691. https://doi.org/10.1074/jbc.M807050200.

Huang, Y., Roth, B., Lü, W., and Du, J. (2019). Ligand recognition and gating mechanism through three ligand-binding sites of human TRPM2 channel. eLife *8*, e50175. https://doi.org/10.7554/eLife.50175.

Jia, J., Verma, S., Nakayama, S., Quillinan, N., Grafe, M.R., Hurn, P.D., and Herson, P.S. (2011). Sex differences in neuroprotection provided by inhibition of TRPM2 channels following experimental stroke. J. Cereb. Blood Flow Metab. *31*, 2160–2168. https://doi.org/10.1038/jcbfm.2011.77.

Jiang, J., Li, M., and Yue, L. (2005). Potentiation of TRPM7 inward currents by protons. J. Gen. Physiol. *126*, 137–150.

Kashio, M., Sokabe, T., Shintaku, K., Uematsu, T., Fukuta, N., Kobayashi, N., Mori, Y., and Tominaga, M. (2012). Redox signal-mediated sensitization of transient receptor potential melastatin 2 (TRPM2) to temperature affects macrophage functions. Proc. Natl. Acad. Sci. USA *109*, 6745–6750. https://doi.org/10.1073/pnas.1114193109.

Lan, J.Y., Skeberdis, V.A., Jover, T., Grooms, S.Y., Lin, Y., Araneda, R.C., Zheng, X., Bennett, M.V., and Zukin, R.S. (2001). Protein kinase C modulates NMDA receptor trafficking and gating. Nat. Neurosci. *4*, 382–390. https://doi.org/10.1038/86028.

Lemasters, J.J., Theruvath, T.P., Zhong, Z., and Nieminen, A.L. (2009). Mitochondrial calcium and the permeability transition in cell death. Biochim. Biophys. Acta *1787*, 1395–1401. https://doi.org/10.1016/j.bbabio.2009.06.009.

Li, Y., and Hao, B. (2010). Structural basis of dimerization-dependent ubiquitination by the SCF(Fbx4) ubiquitin ligase. J. Biol. Chem. *285*, 13896–13906. https://doi.org/10.1074/jbc.M110.111518.

Lipton, P. (1999). Ischemic cell death in brain neurons. Physiol. Rev. *79*, 1431–1568. https://doi.org/10.1152/physrev.1999.79.4.1431.

Liu, F., and McCullough, L.D. (2014). The middle cerebral artery occlusion model of transient focal cerebral ischemia. Methods Mol. Biol. *1135*, 81–93. https://doi.org/10.1007/978-1-4939-0320-77.

Longa, E.Z., Weinstein, P.R., Carlson, S., and Cummins, R. (1989). Reversible middle cerebral artery occlusion without craniectomy in rats. Stroke *20*, 84–91.

Luo, J.H., Fu, Z.Y., Losi, G., Kim, B.G., Prybylowski, K., Vissel, B., and Vicini, S. (2002). Functional expression of distinct NMDA channel subunits tagged with green fluorescent protein in hippocampal neurons in culture. Neuropharmacology *42*, 306–318. https://doi.org/10.1016/s0028-3908(01)00188-5.

Mai, C., Mankoo, H., Wei, L., An, X., Li, C., Li, D., and Jiang, L.H. (2020). TRPM2 channel: A novel target for alleviating ischaemia-reperfusion, chronic cerebral hypo-perfusion and neonatal hypoxic-ischaemic brain damage. J. Cell. Mol. Med. *24*, 4–12. https://doi.org/10.1111/jcmm.14679.

Miller, B.A., Wang, J., Hirschler-Laszkiewicz, I., Gao, E., Song, J., Zhang, X.Q., Koch, W.J., Madesh, M., Mallilankaraman, K., Gu, T., et al. (2013). The second member of transient receptor potential-melastatin channel family protects hearts from ischemia-reperfusion injury. Am. J. Physiol. Heart Circ. Physiol. *304*, H1010–H1022. https://doi.org/10.1152/ajpheart.00906.2012.

Mortadza, S.S., Sim, J.A., Stacey, M., and Jiang, L.H. (2017). Signalling mechanisms mediating Zn^{2+}-induced TRPM2 channel activation and cell death in microglial cells. Sci. Rep. *7*, 45032. https://doi.org/10.1038/srep45032.

Nicolai, J., Burbassi, S., Rubin, J., and Meucci, O. (2010). CXCL12 inhibits expression of the NMDA receptor's NR2B subunit through a histone deacetylase-dependent pathway contributing to neuronal survival. Cell Death Dis. *1*, e33. https://doi.org/10.1038/cddis.2010.10.

Olah, M.E., Jackson, M.F., Li, H., Perez, Y., Sun, H.S., Kiyonaka, S., Mori, Y., Tymianski, M., and MacDonald, J.F. (2009). Ca2+-dependent induction of TRPM2 currents in hippocampal neurons. J. Physiol. *587*, 965–979. https://doi.org/10.1113/jphysiol.2008.162289.

Olney, J.W. (1969). Brain lesions, obesity, and other disturbances in mice treated with monosodium glutamate. Science *164*, 719–721. https://doi.org/10.1126/science.164.3880.719.

Perraud, A.L., Fleig, A., Dunn, C.A., Bagley, L.A., Launay, P., Schmitz, C., Stokes, A.J., Zhu, Q., Bessman, M.J., Penner, R., et al. (2001). ADP-ribose gating of the calcium-permeable LTRPC2 channel revealed by Nudix motif homology. Nature *411*, 595–599.

Perraud, A.L., Schmitz, C., and Scharenberg, A.M. (2003). TRPM2 Ca2+ permeable cation channels: from gene to biological function. Cell Calcium *33*, 519–531. https://doi.org/10.1016/s0143-4160(03)00057-5.

Petit-Pedrol, M., and Groc, L. (2021). Regulation of membrane NMDA receptors by dynamics and protein interactions. J. Cell Biol. *220*, e202006101. https://doi.org/10.1083/jcb.202006101.

Povysheva, N., Nigam, A., Brisbin, A.K., Johnson, J.W., and Barrionuevo, G. (2019). Oxygen-glucose deprivation differentially affects neocortical pyramidal

neurons and parvalbumin-positive interneurons. Neuroscience *412*, 72–82. https://doi.org/10.1016/j.neuroscience.2019.05.042.

Ren, M., Senatorov, V.V., Chen, R.W., and Chuang, D.M. (2003). Postinsult treatment with lithium reduces brain damage and facilitates neurological recovery in a rat ischemia/reperfusion model. Proc. Natl. Acad. Sci. USA *100*, 6210–6215. https://doi.org/10.1073/pnas.0937423100.

Sano, Y., Inamura, K., Miyake, A., Mochizuki, S., Yokoi, H., Matsushime, H., and Furuichi, K. (2001). Immunocyte Ca2+ influx system mediated by LTRPC2. Science *293*, 1327–1330.

Sans, N., Prybylowski, K., Petralia, R.S., Chang, K., Wang, Y.X., Racca, C., Vicini, S., and Wenthold, R.J. (2003). NMDA receptor trafficking through an interaction between PDZ proteins and the exocyst complex. Nat. Cell Biol. *5*, 520–530. https://doi.org/10.1038/ncb990.

Schmitz, C., Perraud, A.L., Johnson, C.O., Inabe, K., Smith, M.K., Penner, R., Kurosaki, T., Fleig, A., and Scharenberg, A.M. (2003). Regulation of vertebrate cellular Mg2+ homeostasis by TRPM7. Cell *114*, 191–200. https://doi.org/10.1016/s0092-8674(03)00556-7.

Schneider, C.A., Rasband, W.S., and Eliceiri, K.W. (2012). NIH Image to ImageJ: 25 years of image analysis. Nat. Methods *9*, 671–675.

Schulien, A.J., Yeh, C.Y., Orange, B.N., Pav, O.J., Hopkins, M.P., Moutal, A., Khanna, R., Sun, D., Justice, J.A., and Aizenman, E. (2020). Targeted disruption of Kv2.1-VAPA association provides neuroprotection against ischemic stroke in mice by declustering Kv2.1 channels. Sci. Adv. *6*, eaaz8110. https://doi.org/10.1126/sciadv.aaz8110.

Scott, D.B., Blanpied, T.A., Swanson, G.T., Zhang, C., and Ehlers, M.D. (2001). An NMDA receptor ER retention signal regulated by phosphorylation and alternative splicing. J. Neurosci. *21*, 3063–3072.

Sena, E., van der Worp, H.B., Howells, D., and Macleod, M. (2007). How can we improve the pre-clinical development of drugs for stroke? Trends Neurosci. *30*, 433–439. https://doi.org/10.1016/j.tins.2007.06.009.

Shimizu, T., Macey, T.A., Quillinan, N., Klawitter, J., Perraud, A.L., Traystman, R.J., and Herson, P.S. (2013). Androgen and PARP-1 regulation of TRPM2 channels after ischemic injury. J. Cereb. Blood Flow Metab. *33*, 1549–1555. https://doi.org/10.1038/jcbfm.2013.105.

Soh, J.W., and Weinstein, I.B. (2003). Roles of specific isoforms of protein kinase C in the transcriptional control of cyclin D1 and related genes. J. Biol. Chem. *278*, 34709–34716. https://doi.org/10.1074/jbc.M302016200.

Soh, J.W., and Weinstein, I.B. (2003). Roles of specific isoforms of protein kinase C in the transcriptional control of cyclin D1 and related genes. J. Biol. Chem. *278*, 34709–34716. https://doi.org/10.1074/jbc.M302016200.

Standley, S., Roche, K.W., McCallum, J., Sans, N., and Wenthold, R.J. (2000). PDZ domain suppression of an ER retention signal in NMDA receptor NR1 splice variants. Neuron *28*, 887–898. https://doi.org/10.1016/s0896-6273(00)00161-6.

Starkus, J.G., Fleig, A., and Penner, R. (2010). The calcium-permeable non-selective cation channel TRPM2 is modulated by cellular acidification. J. Physiol. *588*, 1227–1240. https://doi.org/10.1113/jphysiol.2010.187476.

Thompson, R.J., Zhou, N., and MacVicar, B.A. (2006). Ischemia opens neuronal gap junction hemichannels. Science *312*, 924–927. https://doi.org/10.1126/science.1126241.

Tymianski, M. (2011). Emerging mechanisms of disrupted cellular signaling in brain ischemia. Nat. Neurosci. *14*, 1369–1373. https://doi.org/10.1038/nn.2951.

Virani, S.S., Alonso, A., Benjamin, E.J., Bittencourt, M.S., Callaway, C.W., Carson, A.P., Chamberlain, A.M., Chang, A.R., Cheng, S., Delling, F.N., et al. (2020). Heart disease and stroke Statistics-2020 update: A report from the American Heart Association. Circulation *141*, e139–e596. https://doi.org/10.1161/CIR.0000000000000757.

Wang, L., Fu, T.M., Zhou, Y., Xia, S., Greka, A., and Wu, H. (2018). Structures and gating mechanism of human TRPM2. Science *362*, eaav4809. https://doi.org/10.1126/science.aav4809.

Weilinger, N.L., Lohman, A.W., Rakai, B.D., Ma, E.M., Bialecki, J., Maslieieva, V., Rilea, T., Bandet, M.V., Ikuta, N.T., Scott, L., et al. (2016). Metabotropic NMDA receptor signaling couples Src family kinases to pannexin-1 during excitotoxicity. Nat. Neurosci. *19*, 432–442. https://doi.org/10.1038/nn.4236.

Wu, L.J., Wu, G., Akhavan Sharif, M.R., Baker, A., Jia, Y., Fahey, F.H., Luo, H.R., Feener, E.P., and Clapham, D.E. (2012). The voltage-gated proton channel Hv1 enhances brain damage from ischemic stroke. Nat. Neurosci. *15*, 565–573. https://doi.org/10.1038/nn.3059.

Wu, Q.J., and Tymianski, M. (2018). Targeting NMDA receptors in stroke: new hope in neuroprotection. Mol. Brain *11*, 15. https://doi.org/10.1186/s13041-018-0357-8.

Xie, J., Bi, Y., Zhang, H., Dong, S., Teng, L., Lee, R.J., and Yang, Z. (2020). Cell-penetrating peptides in diagnosis and treatment of human diseases: From preclinical research to clinical application. Front. Pharmacol. *11*, 697. https://doi.org/10.3389/fphar.2020.00697.

Yamamoto, S., Shimizu, S., Kiyonaka, S., Takahashi, N., Wajima, T., Hara, Y., Negoro, T., Hiroi, T., Kiuchi, Y., Okada, T., et al. (2008). TRPM2-mediated Ca2+influx induces chemokine production in monocytes that aggravates inflammatory neutrophil infiltration. Nat. Med. *14*, 738–747. https://doi.org/10.1038/nm1758.

Yan, J., Bengtson, C.P., Buchthal, B., Hagenston, A.M., and Bading, H. (2020). Coupling of NMDA receptors and TRPM4 guides discovery of unconventional neuroprotectants. Science *370*, eaay3302. https://doi.org/10.1126/science.aay3302.

Yan, J.Z., Xu, Z., Ren, S.Q., Hu, B., Yao, W., Wang, S.H., Liu, S.Y., and Lu, W. (2011). Protein kinase C promotes N-methyl-D-aspartate (NMDA) receptor trafficking by indirectly triggering calcium/calmodulin-dependent protein kinase II (CaMKII) autophosphorylation. J. Biol. Chem. *286*, 25187–25200. https://doi.org/10.1074/jbc.M110.192708.

Yang, W., Zou, J., Xia, R., Vaal, M.L., Seymour, V.A., Luo, J., Beech, D.J., and Jiang, L.H. (2010). State-dependent inhibition of TRPM2 channel by acidic pH. J. Biol. Chem. *285*, 30411–30418. https://doi.org/10.1074/jbc.M110.139774.

Zeng, H., Guo, M., Martins-Taylor, K., Wang, X., Zhang, Z., Park, J.W., Zhan, S., Kronenberg, M.S., Lichtler, A., Liu, H.X., et al. (2010). Specification of region-specific neurons including forebrain glutamatergic neurons from human induced pluripotent stem cells. PLoS ONE *5*, e11853. https://doi.org/10.1371/journal.pone.0011853.

Zhang, C., Brown, M.Q., van de Ven, W., Zhang, Z.M., Wu, B., Young, M.C., Synek, L., Borchardt, D., Harrison, R., Pan, S., et al. (2016). Endosidin2 targets conserved exocyst complex subunit EXO70 to inhibit exocytosis. Proc. Natl. Acad. Sci. USA *113*, E41–E50. https://doi.org/10.1073/pnas.1521248112.

Zhang, Z., Tóth, B., Szollosi, A., Chen, J., and Csanády, L. (2018). Structure of a TRPM2 channel in complex with Ca^{2+} explains unique gating regulation. eLife *7*. https://doi.org/10.7554/eLife.36409.

Zheng, X., Zhang, L., Wang, A.P., Bennett, M.V., and Zukin, R.S. (1999). Protein kinase C potentiation of N-methyl-D-aspartate receptor activity is not mediated by phosphorylation of N-methyl-D-aspartate receptor subunits. Proc. Natl. Acad. Sci. USA *96*, 15262–15267. https://doi.org/10.1073/pnas.96.26.15262.

STAR★METHODS

KEY RESOURCES TABLE

REAGENT or RESOURCE	SOURCE	IDENTIFIER
Antibodies		
Rabbit polyclonal antibodies to TRPM2	Novus	Cat#NB110-81601; RRID:AB_1147355
Rabbit polyclonal antibodies to TRPM2 N terminal part	Abmart	Cat#634-1-1-R1
Rabbit polyclonal antibodies to TRPM2 C terminal part	Abmart	Cat#634-2-1-R1
Rabbit polyclonal antibodies to GluN1	Cell Signaling Technology	Cat#5704S; RRID:AB_1904067
Rabbit polyclonal antibodies to GluN2A	Cell Signaling Technology	Cat#4205S; RRID:AB_2112295
Rabbit polyclonal antibodies to GluN2B	Cell Signaling Technology	Cat#4207S; RRID:AB_1264223
Mouse monoclonal antibodies to flag	Sigma-Aldrich	Cat#F3165; RRID:AB_259529
Rabbit polyclonal antibodies to phosphor-CREB(Ser133)	Cell Signaling Technology	Cat#9198S; RRID:AB_2561044
Rabbit polyclonal antibodies to p44/42 MAPK (ERK1/2)	Cell Signaling Technology	Cat#9102S; RRID:AB_330744
Rabbit polyclonal antibodies to phospho-p44/42 MAPK (ERK1/2) (Tyr202/204)	Cell Signaling Technology	Cat#4377T
Rabbit polyclonal antibodies to PKC-γ	Cell Signaling Technology	Cat#59090S; RRID:AB_2799557
Rabbit polyclonal antibodies to Pan-cadherin	Cell Signaling Technology	Cat#4068S; RRID:AB_2158565
Pannexin-1 (D9M1C) Rabbit mAb	Cell Signaling Technology	Cat#91137S; RRID:AB_2800167
Anti-TRPM4 antibody	Abcam	Cat#ab123936; RRID:AB_10976061
Rabbit polyclonal antibodies to GAPDH	Cell Signaling Technology	Cat#2118S; RRID:AB_561053
Rabbit polyclonal antibodies to β-tubulin	Cell Signaling Technology	Cat#2128S; RRID:AB_823664
Rabbit polyclonal antibodies to NeuN	Abcam	Cat#ab187477
Goat anti-rabbit IgG-FITC	Santa Cruz Biotechnology	Cat#sc-2012; RRID:AB_631744
Goat anti-mouse IgG-rhodamine	Thermal Fisher Scientific	Cat#31160
Bacterial and virus strains		
NEB 5-alpha Competent E. coli (High Efficiency)	Biolabs	Cat#C2987U
Chemicals, peptides, and recombinant proteins		
2,3,5-Triphenyltetrazolium chloride	Sigma-Aldrich	Cat#T-8877
N-Methyl-D-aspartic acid	Tocris	Cat#0114
Glutamate	Sigma-Aldrich	Cat#49621
Glycine	Sigma-Aldrich	Cat#50046
Bicuculine	TCI	Cat#B1890
4-Aminopyridine	Sigma-Aldrich	Cat#A-0152
MK-801	Sigma-Aldrich	Cat#M107
Phorbol-12-myristate-13-acetate	Sigma-Aldrich	Cat#524400
30% Hydrogen Peroxide	Thermal Fisher Scientific	Cat#200745
NP40	Thermal Fisher Scientific	Cat#28324
Triton X-100	Sigma-Aldrich	Cat#T-9284
Bovine Serum Albumin	Sigma-Aldrich	Cat#9048-46-8
Goat Serum	Thermal Fisher Scientific	Cat#16210-064
Rhodamine-123	Thermal Fisher Scientific	Cat#R302
Fura-2 AM	Thermal Fisher Scientific	Cat#F1221

(*Continued on next page*)

Continued

REAGENT or RESOURCE	SOURCE	IDENTIFIER
Ionomycin	Sigma-Aldrich	Cat#I0634
Pluronic F-127	Thermal Fisher Scientific	Cat#P3000MP
Proteinase inhibitors	Sigma-Aldrich	Cat#539131-10VL
Phosphatase inhibitors	Thermal Fisher Scientific	Cat#78428
Laemmli Sample Buffer	BIO-RAD	Cat#1610737
Protein A/G PLUS-Agarose	Santa Cruz Biotechnology	Cat#sc-2003
TAT-SC	Genescript	Customized in this study
TAT-EQE	Genescript	Customized in this study
TAT-EE_3	Genescript	Customized in this study
XbaI	BioLabs	Cat#R0145S
XhoI	BioLabs	Cat#R0146S
BamHI	BioLabs	Cat#R3136S
DpnI	BioLabs	Cat#R0176S
KpnI	BioLabs	Cat#R3142S
NotI	BioLabs	Cat#R3189S
EcoRI	BioLabs	Cat#R3101S
T4 DNA ligase	Thermal Fisher Scientific	Cat#2148085
PfuUltra HF	Agilent	Cat#600380-51
Q5 High-Fidelity DNA Polymerase	BioLabs	Cat#M0491S
Dulbecco's Modified Eagle's medium	Thermal Fisher Scientific	Cat#12100-038
Bovine Calf Serum	HyClone	Cat#SH30541.03
Penicillin/streptomycin	Thermal Fisher Scientific	Cat#15140-122
2.5% trypsin	Thermal Fisher Scientific	Cat#15090-046
Neurobasal Medium	Thermal Fisher Scientific	Cat#21103-049
B27 supplement	Thermal Fisher Scientific	Cat#17504-044
Horse serum	Thermal Fisher Scientific	Cat#16050114
L-glutamine	Thermal Fisher Scientific	Cat#25030-081
Cytosine arabinoside	Thermal Fisher Scientific	Cat#C1768
Poly-L-lysine	Sigma-Aldrich	Cat#P4707
Critical commercial assays		
Lipofectamine 3000 Transfection Kit	Thermal Fisher Scientific	Cat#2232162
Pierce Rapid Gold BCA Protein Assay Kit	Thermal Fisher Scientific	Cat#A53225
Pierce Cell Surface Protein Isolation Kit	Thermal Fisher Scientific	Cat#89881
ProteoExtract Native Membrane Protein Extraction Kit	Calbiochem	Cat#444810
Fisher Healthcare Tissue-Plus O.C.T. Compound	Thermal Fisher Scientific	Cat#23-730-571
ProLong Gold Antifade Mountant	Thermal Fisher Scientific	Cat#P10144
QIAprep Spin Miniprep Kit	QIAGEN	Cat#27106
QIAGEN Plasmid Maxi Kit	QIAGEN	Cat#12163
Qiaquick PCR Purification Kit	QIAGEN	Cat#28104
Syn-PER Synaptic Protein Extraction Reagent	Thermal Fisher Scientific	Cat#87793
Q5 Site-Directed Mutagenesis Kit	BioLabs	Cat#E0554S
In Situ Cell Death Detection Kit	Millipore Sigma	Cat#11684795910
Deposited data		
Raw data for western blots	This study	Mendeley Data: https://doi.org/10.17632/wnkmxfd5gc.1

(*Continued on next page*)

Continued

REAGENT or RESOURCE	SOURCE	IDENTIFIER
Experimental models: Cell lines		
293T	ATCC	Cat#CRL-3216
Experimental models: Organisms/strains		
C57B6J mice	JAX laboratory	https://www.jax.org/strain/000664
Trpm2$^{-/-}$ mice	Yamamoto et al., 2008	Dr. Yasuo Mori
TRPM2$^{fl/fl}$ mice	Miller et al., 2013	Dr. Barbara Miller
Nestin-cre mice	JAX laboratory	https://www.jax.org/strain/003771
Oligonucleotides		
Primers for TRPM2 subcloning and mutagenesis, see Table S1	This study	N/A
Primers for GluN2a and GluN2b subcloning and mutagenesis, see Table S1	This study	N/A
Primers for *E. coli* expression, see Table S1	This study	N/A
Recombinant DNA		
GluN1a	Luo et al., 2002	Addgene 17928
GluN2A	Luo et al., 2002	Addgene 17924
GluN2B	Luo et al., 2002	Addgene 17925
PKC-γ	Colgan et al., 2018	Addgene 112266
PKC-γ-DN	Soh and Weinstein, 2003	Addgene 21239
pcDNA4/TO-FLAG-hTRPM2	Perraud et al., 2003	Dr. Sharenberg AM (University of Washington, Seattle)
Software and algorithms		
GraphPad Prism 6.0	GraphPad Software	https://www.graphpad.com/updates/
Biorender	Biorender	N/A
pClamp 9.2	Molecular Devices	https://biorender.com/
Adobe Illustrator	Adobe	https://www.adobe.com/products/illustrator/
NIS Elements AR4	Nikon	https://www.microscope.healthcare.nikon.com/products/software/nis-elements/nis-elements-advanced-research
ImageJ	Schneider et al., 2012	https://imagej.nih.gov/ij/

RESOURCE AVAILABILITY

Lead contact

Further information and requests for resources and reagents should be directed to and will be fulfilled by the lead contact Lixia Yue (lyue@uchc.edu).

Material availability

This study did not generate new unique reagents.

Data and code availability

- Raw data for western blots can be found at Mendeley Data: https://doi.org/10.17632/wnkmxfd5gc.1. Additional data reported in this paper will be shared by the lead contact upon request.
- This paper does not report original code.
- Any additional information required to reanalyze the data reported in this work paper is available from the lead contact upon request.

EXPERIMENTAL MODEL AND SUBJECT DETAILS

Animals

All the experimental mice bred and hosted in the animal facility building of University of Connecticut School of Medicine (UCONN Health) were fed with standard chow diet and water ad libitum. Standard housing conditions were maintained at a controlled temperature with a 12-h light/dark cycle. All experimental procedures and protocols were approved by the Institutional Animal Care and Use Committee (IACUC) of University of Connecticut School of Medicine (animal protocol: AP-200135-0723), and were conducted in accordance with the U.S. National Institutes of Health Guidelines for the Care and Use of Laboratory Animals. Male mice at 8 to 12 weeks old were used in this study.

The global TRPM2 knockout (TRPM2-KO, or gM2KO) mice were generated by Dr. Yasuo Mori's lab at Kyoto University Japan. The deletion of *Trpm2* was developed in C57B6J mouse by replacing the third exon (S5–S6 linker in the pore domain) with a neomycin coding region. The knockout mice exhibited no differences in behavior or impairment in breeding, compared to wild type (WT) C57BJ6 mice (Yamamoto et al., 2008). TRPM2-KO mice were back-crossed to C57BL/6 mice for $\geq$10 generations before being used for experiments.

The neuron specific knockout of TRPM2 (nM2KO) was generated by breeding $TRPM2^{fl/fl}$ mice with Nestin-Cre ((B6.Cg-Tg)Nes-cre) 1kln/J: 003771; JAX laboratory). $TRPM2^{fl/fl}$ mice were generated by Dr. Barbara Miller (Miller et al., 2013) (Penn State University, Pennsylvania). The exons 21 and 22 encoding transmembrane domain 5 and 6 and pore loop were flanked by loxp recombination sites and will be deleted by Cre recombinase (Miller et al., 2013). The mice were backcrossed with C57BL/6 mice for $\geq$10 generations before being used for experiments. The $TRPM2^{flox/flox}$ ($TRPM2^{fl/fl}$) with Cre^{+} mice and $TRPM2^{fl/fl}$ with Cre^{-} mice from the same litters were paired for experiments throughout the manuscript.

The inducible global knockout was also generated by using $TRPM2^{fl/fl}$ mice breeding with global Cre, Rosa26-CreERT2 (B6.129-$Gt(ROSA)26Sor^{tm1(cre/ERT2)Tyj}$/J: 008463; JAX laboratory). Knockout was induced by Tamoxifen treatment and confirmed by genotyping. The mice were backcrossed with C57BL/6 mice for $\geq$10 generations before being used for experiments.

Cortical neuron isolation and culture

Mice pups at P0 were euthanized based on animal protocol. Whole brain was dissected out immediately and immersed in ice-cold Hank's Balanced Salt Solution (HBSS). Meninges were removed thoroughly, and tissue of different brain areas was taken based on purposes. Brain tissue was cut into small pieces and digested with 0.25% trypsin (Thermal Fisher Scientific, 15090-046) in HBSS at 37 °C for 20 min. Digestion solution was quickly removed, and tissue pellets are washed with Neurobasal Medium (Thermal Fisher Scientific, 21103-049) for 3 times. Cells were resuspended with appropriate amount of Neurobasal Medium supplemented with 2% B27 supplement (Thermal Fisher Scientific, 17504-044), 3% horse serum (Thermal Fisher Scientific, 16050114), 0.25% L-glutamine (Thermal Fisher Scientific, 25030-081) and 1% penicillin/streptomycin (Thermal Fisher Scientific, 15140-122). Isolated cells were counted and plated on coverslips pre-coated with poly-L-lysine (Sigma-Aldrich, P4707) at a density of about 500 x 10^3 cells/cm^2 for OGD and H_2O_2 treatment, and 100 x 10^3 cells/cm^2 for current recording. Cytosine arabinoside (Sigma-Aldrich, C1768) was added to maintain a concentration at 1 μM to inhibit the proliferation of non-neuronal cells. 24 h after plating, culture medium was changed to Neurobasal Medium supplemented with 2% B27 supplement, 0.25% L-glutamine and 1% penicillin/streptomycin. The concentration of Cytosine arabinoside (araC) was increased to 2 μM. Medium was changed every 3 days. OGD and H_2O_2 treatment was conducted at 7^{th} day of culture, and current recording was conducted at 7^{th}, 10^{th} and 14^{th} day of culture.

Cell line culture and transfection

HEK293T cells were cultured in Dulbecco's Modified Eagle's medium (DMEM) (Thermal Fisher Scientific, 12100-038) supplemented with 10% BGS (HyClone, SH30541.03) and 0.5% penicillin/streptomycin (Thermal Fisher Scientific, 15140-122) at 37 °C and 5% CO2. 8h prior to transfection, culture medium was replaced with DMEM supplemented only with 2.5% BGS. Cells were transfected when at a confluence about 80-90% using Lipofectamine 3000 Transfection Kit (Thermal Fisher Scientific, 2232162) based on instruction.

METHOD DETAILS

Middle cerebral artery occlusion (MCAO)

Eight- to nine-week-old male mice (~25 g) were subjected to right middle cerebral artery occlusion (MCAO) for 120 min followed by 24 hours of reperfusion, or MCAO for 60 min followed by 7-days reperfusion. The genotype information was blinded to the surgeon who conduct the surgeries. MCAO surgery was performed as previously described (Liu and McCullough, 2014; Wu et al., 2012). In brief, mice were anesthetized with 2% isoflurane (vol/vol) in 100% oxygen and the anesthesia was maintained with 1.5% isoflurane during surgery through nose cone (Harvard Apparatus). The unilateral right middle cerebral artery (MCA) occlusion was carried out by advancing a silicone-coated 6-0 monofilament (Doccol Corporation, Sharon, MA) 10 to 11 mm from internal carotid artery bifurcation via an external carotid artery incision (Chiang et al., 2011). Mouse body temperature was monitored by a rectal temperature probe and maintained at ~37°C with an automatic temperature-regulating heating pad connected to animal temperature controller (TCA T-2DF, Physitemp). Cerebral blood flow was monitored after occlusion as well as after reperfusion. The bregma was exposed and the skull bone countersunk at two 3 × 3-mm areas over both MCA supply territories for bilateral monitoring of local cortical blood flow. Successful occlusion was

confirmed by 85% reduction of cerebral blood flow monitored using laser Doppler blood FlowMeter (Moor-VMS-LDF1, Moor Instrument, Dever, UK). Sham control mice underwent the same procedure but without insertion of filament to occlude the MCA.

Neurological deficit score evaluation

Neurological deficit was scored based on previously reported criteria (Longa et al., 1989). In brief, score 0 represents no neurological deficit; score 1 represents failure to extend left paw; Score 2 represents circling to the left; score 3 represents falling to the left; score 4 represents inability of spontaneously walking and decreased level of consciousness; and score 5 represents death due to brain ischemia. The observer to score the neurological deficit was an experienced observer and blinded by the group assignment and genotype information. If the animal score was 0 or 5, it was removed from the study.

Rotarod test

For examining the long-term protective effect of TAT-EE3, motor coordination of mice was evaluated by rotarod test right after the evaluation of neurological deficit score at 1st, 3rd, and 7th day after MCAO. Briefly, mice were placed on a rotating rod with the speed range of 6-56 rounds per minute for 5 minutes. Each mouse was tested for 3 times with two 20-min interval in between. The falling from the rotating rod was recorded and the averaged latency of each mouse was used for quantification.

Infarct volume assessment by Triphenyl Tetrazolium chloride (TTC) staining

Tetrazolium chloride (Sigma-Aldrich, T-8877) was dissolved in PBS at a concentration of 20 mg/ml 30 min prior to use. Post-stroke mice were euthanized and brains were frozen at -80°C for 5 min, cut into coronary slices at a thickness of 1 mm. Brain slices were stained with 2% TTC (vol/vol) for 20 min, and then washed using PBS for 3 times, and fixed in 10% Neutral *buffered* formalin for later scanning. TTC labels non-injured tissue, leaving the infarct area white. The stained slices were scanned for data analysis using ImageJ software. The infarct volume was calculated and presented as a percentage of total brain volume as previously reported (Ren et al., 2003; Schulien et al., 2020).

Antibodies, chemicals, and reagents

Rabbit polyclonal antibodies to TRPM2 (Novus, NB110-81601, 1:500 in 5% BSA for WB, 1:50 in protein extraction for IP); Rabbit polyclonal antibodies to GluN1 (Cell Signaling Technology, 5704S, 1:1000 in 5% BSA for WB, 1:50 in protein extraction for IP); Rabbit polyclonal antibodies to GluN2A (Cell Signaling Technology, 4205S, 1:1000 in 5% BSA for WB, 1:50 in protein extraction for IP). Rabbit polyclonal antibodies to GluN2B (Cell Signaling Technology, 4207S, 1:1000 in 5% BSA for WB, 1:50 in protein extraction for IP); Mouse polyclonal antibodies to flag (Sigma-Aldrich, F3165, 1:5000 in 5% BSA for WB): Rabbit polyclonal antibodies to GFP (Cell Signaling Technology, 2956S, 1:2000 in 5% BSA for WB); Rabbit polyclonal antibodies to CREB (Cell Signaling Technology, 4820S, 1:2000 in 5% BSA for WB); Rabbit polyclonal antibodies to phosphor-CREB(Ser133) (Cell Signaling Technology, 9198S, 1:2000 in 5% BSA for WB); Rabbit polyclonal antibodies to p44/42 MAPK (ERK1/2) (Cell Signaling Technology, 9102S, 1:2000 in 5% BSA for WB); Rabbit polyclonal antibodies to phospho-p44/42 MAPK (ERK1/2) (Tyr202/204) (Cell Signaling Technology, 4377T, 1:2000 in 5% BSA for WB); Rabbit polyclonal antibodies to PKC-γ (Cell Signaling Technology, 59090S, 1:5000 in 5% BSA for WB); Rabbit polyclonal antibodies to Pan-cadherin (Cell Signaling Technology, 4068S, 1:5000 in 5% BSA for WB); Rabbit polyclonal antibodies to TRPM4 (abcam, ab123936, 1:5000 in 5% BSA for WB); Rabbit polyclonal antibodies to pannexin-1 (Cell Signaling Technology, 91137S, 1:5000 in 5% BSA for WB); Rabbit polyclonal antibodies to GAPDH (Cell Signaling Technology, 2118S, 1:5000 in 5% BSA for WB); Rabbit polyclonal antibodies to β-tubulin (Cell Signaling Technology, 4820S, 1:5000 in 5% BSA for WB); Mouse monoclonal antibodies to Caspase-3 (Santa Cruz Biotechnology, sc-7272, 1:1000 in 5% BSA for WB, 1:50 in 5% BSA and 15% goat serum for immunofluorescence staining); Rabbit polyclonal antibodies to NeuN (Abcam, ab187477, 1:50 in 5% BSA and 15% goat serum for immunofluorescence staining); Goat anti-rabbit IgG-FITC (Santa Cruz Biotechnology, sc-2012, 1:1000 in 5% BSA and 15% goat serum for immunofluorescence staining); Goat anti-mouse IgG-rhodamine (Thermal Fisher Scientific, 31660, 1:1000 in 5% BSA and 15% goat serum for immunofluorescence staining); Prolong Gold antifade reagent with DAPI (Life technologies, P36935), HRP-linked anti-rabbit IgG (Cell Signaling Technology, 7074S, 1:10000 in 5% BSA for WB); HRP-linked anti-mouse-IgG (Cell Signaling Technology, 7076S, 1:10000 in 5% BSA for WB); Tetrazolium chloride (Sigma-Aldrich, T-8877); NMDA (Tocris, 0114); Glutamate (Sigma-Aldrich, 49621); Glycine(Sigma-Aldrich, 50046); Bicuculine (TCI, B1890); 4-AP (Sigma-Aldrich, A-0152); MK-801 (Sigma-Aldrich, M107); PMA (Sigma-Aldrich, 524400); 4-α-PMA (Sigma-Aldrich, P128); H_2O_2 (Thermal Fisher Scientific, 200745); BAPTA (Cayman chemical, 11706); BAPTA-AM (Cayman chemical, 15551); Mn(III)TBAP (chloride) (Cayman chemical, 75850); L-NNA (Cayman chemical, 80220); NP40 (Thermal Fisher Scientific, 28324); Triton X-100 (T-9284), Bovine Serum Albumin (Sigma-Aldrich, 9048-46-8), Goat Serum (Thermal Fisher Scientific, 16210-064). All chemicals for making artificial cerebrospinal fluid (aCSF; see below) and recording solution (see below) were purchased from Sigma-Aldrich.

Membrane permeable peptide TAT-EE$_3$ for disrupting TRPM2 and NMDARs coupling and scramble control TAT-SC peptides

TAT-SC (sequence: YGRKKRRQRRR VILLKDHTLEYPVF), TAT-EQE (sequence: YGRKKRRQRRR EEDTDSSQQMLALAEE), TAT-EE$_3$ (sequence: YGRKKRRQRRR EEDTDSSEEMLALAEE) were ordered from GenScript Biotech, and dissolved in PBS to make a stock concentration at 10 mM. HEK-293T cells or isolated neurons were treated with TAT-SC or TAT-EE$_3$ at a concentration

of 10 μM for at least 8h prior to use. Mice were intraperitoneal injected (ip) with TAT-SC or TAT-EE_3 at a dose of 100 nmol/kg. Detailed injection strategy is described in Figure 8B.

Plasmids and enzymes

GluN1a (Addgene, 17928), GluN2A (Addgene, 17924), GluN2B (Addgene, 17925), PKC-γ (Addgene, 112266), PKC-γ-DN (Addgene, 21239). The pcDNA4/TO-FLAG-hTRPM2 construct was a kind gift from Dr. Sharenberg AM (University of Washington, Seattle) (Perraud et al., 2003).

XbaI (BioLabs, R0145S), BamHI (BioLabs, R3136S), XhoI (BioLabs, R0146S), DpnI (BioLabs, R0176S), EcoRI (BioLabs, R3101S), KpnI (BioLabs, R3142S), NotI (BioLabs, R3189S) and T4 DNA ligase (Thermal Fisher Scientific, 2148085), PfuUltra HF (Agilent, 600380-51), and Q5 High-Fidelity DNA Polymerase (Biolabs, M0491S) were used to generating different deletion or mutation constructs.

Subcloning

For TRPM2, subcloning of N terminus (1-727) was achieved by introducing a stop codon (A2282T) by PCR using PfuUltra HF. C terminal of TRPM2 was amplified by PCR using Q5 High-Fidelity DNA Polymerase, cut by EcoRI and XbaI, and inserted into EGFP-C3 vector. To look for the binding part in N terminus of TRPM2, a series of stop codons were introduced by PCR using PfuUltra HF (C1831A, C1994T, G2138T, A2090T). EE_3 motif was deleted by PCR using Q5 High-Fidelity DNA Polymerase. EE was mutated to QQ by PCR using PfuUltra HF (G2093C, G2096C; G2117C, G2120C; G2138C, G2141C). For GluN2A and GluN2B, C terminal was amplified by PCR using Q5 High-Fidelity DNA Polymerase, cut by EcoRI and XbaI, and inserted into EGFP-C3 vector. Deletion of C terminus of GluN2a and GluN2b were achieved by introducing a stop codon by PCR using PfuUltra HF (G4371T for GluN2B and G4518T for GluN2B). Deletion of the KKR motif in GluN2a and GluN2b were achieved by PCR using Q5 Site-Directed Mutagenesis Kit based on the instruction.

For *E. coli* expression system, EE_3 containing segment and EQE containing segment In TRPM2 were amplified by PCR using Q5 High-Fidelity DNA Polymerase, cut by KpnI and NotI, and inserted into a homemade His_6-tagged vector; and KKR containing segment in GluN2a and GluN2b were amplified by PCR using Q5 High-Fidelity DNA Polymerase, cut by KpnI and NotI, and inserted into a homemade GST-tagged vector. The information of all the primers is listed in the Table S1.

E. coli expression and purification of proteins

The human GluN2a and GluN2b genes were cloned into a modified pGEX vector containing a removable tobacco etch virus (TEV) protease recognition site. The GluN2a (residues 1208 – 1317; MW: 16.7 kDa) and GluN2b (residues 1212 – 1322; MW: 16.7 kDa) proteins were expressed in Escherichia coli BL21(DE3) cells grown to an OD600 (optical density at 600 nm) between 0.8-1.0 at 37°C followed by induction of protein expression at 21°C overnight using 0.5 mM isopropyl-D-1-thiogalactopyranoside (IPTG). Cells were harvested by centrifugation, resuspended by lysis buffer containing 25 mM Tris-HCl (pH 8.0), 200 mM NaCl, 1% phenylmethylsulfonyl fluoride (PMSF) and 2 mM dithiothreitol (DTT), and lysed by using high-pressure homogenization (Avestin EmulsiFlex C3). The lysates were clarified by centrifugation at 30,000 rpm at 4°C for 30 min, and the supernants were applied to a Glutathione Sepharose 4B column (GE Healthcare). After being extensively washed with lysis buffer, the GST-tagged GluN2a and GluN2b fusion proteins were eluted with a buffer containing 25 mM Tris-HCl (pH 8.0), 200 mM NaCl, 15 mM reduced glutathione and 2 mM DTT. The proteins were concentrated using an Amicon stirred ultrafiltration cell unit with a 10-kDa cutoff membrane (EMD Millipore) and stored at -80°C until use.

The human wild-type TRPM2 (residues 644–760; ∼ 16.7 kDa) and its EQE mutant were cloned into a modified pET15b vector containing a removable TEV protease recognition site. The proteins were expressed in E. coli BL21(DE3) as described above. Cell pellets were resuspended in denaturing buffer containing 25 mM Tris-HCl (pH 8.0), 300 mM NaCl, 1% PMSF and 6 M Urea and lysed by high-pressure homogenization. The lysates were clarified by centrifugation at 30,000 rpm at 4 °C for 30 min, and the supernants were applied to a Ni^{2+}-nitrilotriacetic acid (NTA) column (GE Healthcare). After being extensively washed with 25 mM imidazole in the denaturing buffer, the His_6-tagged TRPM2 fusion proteins were eluted with a buffer containing 25 mM Tris-HCl (pH 8.0), 300 mM NaCl and 250 mM imidazole. To refold the TRPM2 proteins, the denatured samples were dialyzed at 4 ° C overnight against two changes of a buffer without urea [25 mM Tris-HCl (pH 8.0), 200 mM NaCl and 2 mM DTT]. The protein solutions were concentrated using an Amicon stirred ultrafiltration cell unit with a 10-kDa cutoff membrane and stored at -80°C until use.

In vitro protein-protein direct binding assay

About 1∼10 μg of purified proteins were added into 1 mL freshly prepared binding buffer (25 mM HEPES, 100 mM NaCl, 0.01% Triton X-100 and 5% glycerol) for *in vitro* direct binding at 4 °C for overnight. Then Co-immunoprecipitation assay was performed using either anti-GST or anti-His antibodies at 1:50 dilution as detailed described in the Co-immunoprecipitation section. The precipitated proteins were detected by coommassie blue staining and western blot.

Oxygen-glucose deprivation

Oxygen-glucose deprivation (OGD) was achieved by replace the glucose in aCSF with sucrose, and 95% N_2 and 5% CO_2 was used to equilibrate sucrose-aCSF to displace oxygen (Povysheva et al., 2019; Weilinger et al., 2016). This condition typically yielded a pO_2 of < 5 mm Hg in the imaging chamber (Thompson et al., 2006). At least 10 min was allowed for neurons to adapt to the change from culture medium to aCSF before OGD was applied.

Real-time monitoring of mitochondrial function

Mitochondria function was evaluated using Rhodamine-123 dequenching as previously reported. Rhodamine-123 (Rh123, Thermal Fisher Scientific, R302) was dissolved in DMSO to make a stock concentration at 10 mg/ml. Pre-warmed Neurobasal Medium was used to dilute Rhodamine-123 to 5 μg/ml as working concentration. Culture medium was removed and cultured neurons on the 25 mm coverslip were washed using prewarmed PBS for 3 times, then 2 ml of Rh123 working solution was added. Cells were incubated with Rh123 at 37 °C for 5 min. Then Rh123 working solution was replaced with culture medium. At least 10 min were allowed to achieve Rh123 equilibration after the transition of culture medium to aCSF before experiments.

Fluorescence intensities at 509 nm with excitation at 488nm was collected every 15 s for 30 min using CoolSNAP HQ2 (Photometrics) and data were analyzed using NIS-Elements (Nikon).

Ratio calcium imaging experiments

Changes of intracellular Ca^{2+} was measured using ratio Ca^{2+} imaging as we described previously (Du et al., 2010). In brief, Fura-2 AM (Thermal Fisher Scientific, F1221) was dissolved in DMSO to make a stock concentration at 1 mM. Pre-warmed Neurobasal Medium (Thermal Fisher Scientific, 21103-049) was used to dilute Fura-2 AM to a working concentration at 2.5 μM, and 0.02% Pluronic F-127 (Thermal Fisher Scientific, P3000MP) was added to facilitate loading of Fura-2 AM. Cells plated on 25 mm glass coverslips were washed using pre-warmed PBS for 3 times, and then incubated with 2 ml of Fura-2 AM working solution for 30∼45 min at 37 °C. Non-incorporated dye was washed away using HEPES-buffered Saline Solution (HBSS) containing (in mM): 20 HEPES, 10 glucose, 1.2 $MgCl_2$, 1.2 KH_2PO_4, 4.7 KCl, 140 NaCl, 1.3 Ca^{2+} (pH 7.4).

Ca^{2+} influx was measured by perfusing the cells with Tyrode's solution for transfected HEK293T cells or aCSF for neurons under different conditions. Ionomycin (Iono) at 1 μM was applied at the end of the experiment as an internal control. Fluorescence intensities at 510 nm with 340 nm and 380 nm excitation were collected at a rate of 1 Hz using CoolSNAP HQ2 (Photometrics) and data were analyzed using NIS-Elements (Nikon). The 340:380 nm ratio in the presence of different treatments was normalized to the maximal Ca^{2+} signal elicited by 1 μM Ionomycin (Iono) as we previously reported (Du et al., 2010).

Recording of extracellular NMDAR mediated calcium influx was performed as reported by Dr. Hilmar Bading previously (Bengtson et al., 2008; Hardingham et al., 2002). Briefly, bicuculine (Bic, 50 μM) and 4-Aminopyridine (4-AP, 2.5 mM) in the presence of glycine (10 μM) were used to promote synaptic glutamate release and to induce the AP burst for 3 min. Then in the background of AP bursting, MK-801 (10μM), an activity-dependent NMDA receptor blocker, was applied to block synaptic NMDA receptor. After 10 min, neurons were washed using aCSF with tetrodotoxin (TTX, 1 μM) to block synaptic activities for 5 min. Then neurons were washed using aCSF for 2 min and NMDA (100 μM) was applied to induce Ca^{2+} influx mediated by extrasynaptic NMDA receptor in the presence of glycine (10 μM) and in the absence of Mg^{2+}.

Co-immunoprecipitation

NP-40 lysis buffer (10% NP40, 150 mM NaCl, 1 mM EDTA, 50 mM Tris, pH=8.0) containing proteinase inhibitors (Sigma-Aldrich, 539131-10VL) and phosphatase inhibitors (Thermal Fisher Scientific, 78428) was used to lyse both cultured cells and frozen brain tissue. For transfected cells, proteins were extracted 36 hours after transfection. Cell and tissue lysate were lysed by ultrasound using an ultrasonic cleaner (Thermal Fisher Scientific) filled with ice-cold water for 30 min. After incubated on ice for 1 h, lysate was centrifuged at 13000 g for 30 min and supernatant was collected. Protein concentration was measured using Pierce Rapid Gold BCA Protein Assay Kit (Thermal Fisher Scientific, A53225). 300 μg of protein was taken and diluted using NP-40 lysis buffer to make a total volume of 500 μl. Unused protein was allocated and frozen at -80 °C for future use. Appropriate amount of antibody was added based on instruction. After protein-antibody mixture was incubated on ice for 2 h, 25 μl of pre-washed Protein A/G PLUS-Agarose (Santa Cruz Biotechnology, sc-2003) was added, and the whole mixture was incubated at 4 °C for overnight. Then the mixture was centrifuged at 2500g for 1min to get agarose beads. Agarose beads was washed using NP-40 lysis buffer for 7 times, mixed with same amount of 2x Laemmli Sample Buffer (BIO-RAD, 1610737), and boiled at 95 °C for 5 min. Then samples were ready for western blotting analysis.

Western blotting

NP-40/Triton lysis buffer (10% NP40, 1% Triton X-100, 150 mM NaCl, 1 mM EDTA, 50 mM Tris, pH=8.0) containing proteinase inhibitors and phosphatase inhibitors was used to lyse both cultured cells and frozen brain tissue. Surface protein was extracted using Pierce Cell Surface Protein Isolation Kit (Thermal Fisher Scientific, 89881) in transfected HEK-293T cells, and using ProteoExtract Native Membrane Protein Extraction Kit (Calbiochem, 444810) in brain tissue based on instructions. Synaptosome was isolated using the Syn-PER Synaptic Protein Extraction Reagent (Thermal Fisher Scientific, 87793). For transfected cells, proteins were extracted 36 hours after transfection. Cell and tissue lysate were lysed by ultrasound using an ultrasonic cleaner filled with ice-cold water for 30 min. After incubated on ice for 1 h, lysate was centrifuged at 13000 g for 30 min and supernatant was collected. Protein concentration was measured using Pierce Rapid Gold BCA Protein Assay Kit.

30-50 μg of total protein was loaded and separated proteins were transferred to Nitrocellulose membranes. Membranes were blocked with 5% BSA and 2.5% goat serum in Tris buffered saline (TBS, pH=7.4) at room temperature for 2 h, and incubated with primary antibodies in TBS with 0.05% Tween (TBS-T) at room temperature for 2 h. Then membranes were incubated with secondary antibodies in TBS-T for 1 h at room temperature for 1 h for detection. Blots were developed with ImageQuant LAS 4000 imaging system. Band intensity was quantified using ImageJ software and normalized with appropriate loading controls.

Electrophysiology

Whole cell currents were recorded using an Axopatch 200B amplifier. Data were digitized at 10 or 20 kHz and digitally filtered offline at 1 kHz. Patch electrodes were pulled from borosilicate glass and fire-polished to a resistance of ~3 MΩ when filled with internal solutions. Series resistance (R_s) was compensated up to 90% to reduce series resistance errors to <5 mV. Cells in which R_s was >10 MΩ were discarded (Du et al., 2009b).

For heterologous expression, transfected HEK-293 cells were identified by GFP fluorescence. TRPM2 current recording in transfected HEK-293T cells was performed as we previously reported (Du et al., 2009a, 2009b). TRPM2 and NMDAR currents recordings from cultured neurons were performed using aCSF as extracellular solution as we previously reported (Zeng et al., 2010). In brief, for TRPM2 current recordings, voltage stimuli lasting 250 ms were delivered at 1-s intervals, with voltage ramps ranging from −100 to +100 mV at holding potential of 0 mV to elicited currents. For NMDAR current recordings, a gap-free protocol at holding potential of -80 mV was applied to elicit NMDA currents upon agonist stimulation. A fast perfusion system was used to exchange extracellular solutions and to deliver agonists and antagonists to the cells, with a complete solution exchange achieved in about 1–3 s (Jiang et al., 2005).

Normal Tyrode solution for current recording in HEK-293 cells contained (mM): 145 NaCl, 5 KCl, 2 $CaCl_2$, 10 HEPES, 10 glucose, osmolarity=290-320 mOsm/Kg, and pH=7.4 was adjusted with NaOH. Extracellular solution for current recording in neuron, the aCSF solution contained (mM):124 NaCl, 2.5 KCl, 2 $MgSO_4$, 2 $CaCl_2$, 1.2 NaH_2PO_4, 24 $NaHCO_3$, 5 HEPES, 12.5 glucose, osmolarity=300-310 mOsm/Kg, with pH=7.4 adjusted with NaOH. For oxygen-glucose-deprivation (OGD) solution, glucose was eliminate from extracellular solution, and the solution was saturated with nitrogen (N_2) bubbling for 30 min before the experiments.

The internal pipette solution for whole cell current recordings of TRPM2 overexpressed in HEK293 cells (pipette solution-1: P1) contained (in mM): 135 Cs-methanesulfonate ($CsSO_3CH_3$), 8 NaCl, 0.5 $CaCl_2$, 1 EGTA, and 10 HEPES, with pH adjusted to 7.2 with CsOH. Free $[Ca^{2+}]_i$ buffered by EGTA was ~ 100 nM calculated using Max chelator (Du et al., 2009b). ADPR 200 μM was included in the pipette solution for most experiments. The intracellular pipette solution to test the effects of OGD on TRPM2 currents in neuron was adjusted to sub-optimal condition (pipette solution-2: P2), containing (in mM) 135 $CsSO_3CH_3$, 8 NaCl, 3 $MgCl_2$ and 10 HEPES (pH 7.2) with 5 μM EGTA and 1 μM ADPR. Free $[Ca^{2+}]_i$ buffered by EGTA was ~ 500 nM calculated using Max chelator.

The intracellular solution for NMDAR current recording (pipette solution-3: P3) contained (mM): 110 K-ASP, 20 KCl, 1 $MgSO_4$, 10 mM BAPTA, 0.1 GTP, 5 ATP-Mg_2, 10 HEPES, osmolarity=275-285 mOsm/Kg, pH=7.2 adjusted with KOH. For the experiments using cells pretreated with the disrupting peptides TAT-SC and TAT-EE_3, 10 μM TAT-SC or TAT-EE_3 or TAT-EQE was included in the pipette solution, and at least 10 min was allowed for achieving intracellular equilibration of TAT-SC or TAT-EE_3 before current recording.

For current recordings in neurons, tetrodotoxin (0.5 μM) was included in the external solution to block voltage-gated Na^+ current, and 10 μM nifedipine was used to block voltage-gated Ca^{2+} currents for recording TRPM2 currents.

The above-mentioned pipette solutions and extracellular solutions were specific for TRPM2 or NMDAR current recordings, without "cross-contamination" for each other or from other channel activation. The omitting of ADPR and including high concentration of potent calcium chelator in the pipette solution for NMDAR current recordings eliminated any possibility of TRPM2 channel activation because TRPM2 requires Ca^{2+} and ADPR to be activated. No Ca^{2+} pipette solution for NMDAR current recording also prevented other Ca^{2+}-activated currents such as TRPM4. Moreover, using $CsSO_3CH_3$ in the pipette solution for TRPM2 current recordings eliminated contamination from any potassium channels for recordings in neurons and in HEK-293 cells.

Immunofluorescence staining

Brains harvested from mice were frozen at -80 °C prior to use, and was mounted in Fisher Healthcare Tissue-Plus O.C.T. Compound (Thermal Fisher Scientific, 23-730-571) prior to cutting. Brains were cut into sagittal slices at a thickness of 6 to 8 μm, mounted to Superfrost Plus Microscope Slides (Thermal Fisher Scientific, 12-550-15), and frozen at -80 °C for future use. Prior to staining, slides were taken to room temperature for at least 30 min allowing for dehydration. Slices were fixed in 10% formaldehyde for 15 min following washing using PBS for 3 times, and incubated in blocking solution containing 5% BSA, 15% goat serum and 1% Triton X-100 at room temperature for 2 h. Primary antibodies were diluted as described previously in TBS-T containing 15% goat serum. Slices were incubated with primary antibodies for at least 12 h at 4 °C following washing using PBS for 3 times, and incubated with secondary antibodies at room temperature for 2 h. Then slices were washed using PBS for 3 times, and mounted using Prolong Gold anti-fade reagent with DAPI. Slices were kept at 4 °C before taking pictures. TUNEL staining was performed based on the instruction of kit at the penumbra areas (Figure S1N).

QUANTIFICATION AND STATISTICAL ANALYSIS

Data analysis was done by experimenters blind to experimental conditions. All data are expressed as mean ± SEM. For two groups' comparison, statistical significance was determined using Student's t-test. For multiple groups' comparison, statistical significance was determined using one-way or two-way analysis of variance (ANOVA) followed by Bonferroni posttest. Distribution of the data was analyzed prior to analysis to determine whether the data met assumptions of the statistical approach. $p<0.05$ was regarded as significant. The exact sample size and related information can be found in the figure legends.